https://doi.org/10.5194/egusphere-2026-3265
Preprint. Discussion started: 19 June 2026

Microphysical Properties and Ice Crystal Habits of Low-Level Arctic Mixed-Phase Clouds from Four Airborne In Situ Campaigns over the Svalbard Seas

Aymeric Dziduch[1], Antoine Baudoux[1], Guillaume Mioche[1], Antoine Canzi[1], Benjamin Doiteau[1], Manuel Moser[2], Emma Järvinen[3], Étienne Vignon[4], Jean-Christophe Raut[5], Régis Dupuy[1], Christophe Gourbeyre[1], Jean-Luc Baray[1], Marie Monier[1], Frédéric Szczap[1], Guillaume Penide[6], Julien Delanoë[5], Odran Sourdeval[6], Alfons Schwarzenboeck[1], Stephan Mertes[7], Franz Martin Schnaiter[3,8], Christiane Voigt[2,9], Mario Mech[10], Susanne Crewell[10], Andreas Herber[11], Christof Lüpkes[11], André Ehrlich[12], Manfred Wendisch[12], and Olivier Jourdan[1]

[1]Laboratoire de Météorologie Physique (LaMP)/OPGC, Université Clermont Auvergne, CNRS/UMR 6016, Clermont-Ferrand, France
[2]Institut für Physik der Atmosphäre, Deutsches Zentrum für Luft- und Raumfahrt, Weßling, Germany
[3]Institute for Atmospheric and Environmental Research, University of Wuppertal, Wuppertal, Germany
[4]Laboratoire de Météorologie Dynamique-IPSL, Sorbonne Université/CNRS/Ecole Normale Supérieure-PSL Université/Ecole Polytechnique-Institut Polytechnique de Paris, Paris, France
[5]Laboratoire, Atmosphères, Observations Spatiales (LATMOS)/IPSL, Sorbonne Université, UVSQ, CNRS, Paris, France
[6]Laboratoire d'Optique Atmosphérique (LOA), Université de Lille, CNRS, UMR 8518, Lille, France
[7]Abteilung Atmosphärische Mikrophysik, Leibniz-Institut für Troposphärenforschung, Leipzig, Germany
[8]schnaiTEC GmbH, Wuppertal, Germany
[9]Institut für Physik der Atmosphäre, Johannes Gutenberg-Universität, Mainz, Germany
[10]Institut für Geophysik und Meteorologie, Universität zu Köln, Cologne, Germany
[11]Alfred-Wegener-Institut, Helmholtz-Zentrum für Polar- und Meeresforschung, Bremerhaven, Germany
[12]Leipziger Institut für Meteorologie, Universität Leipzig, Leipzig, Germany

Correspondence: Aymeric Dziduch (Aymeric.Dziduch@uca.fr) and Olivier Jourdan (Olivier.Jourdan@uca.fr)

Abstract. This study presents a statistical analysis of the microphysical properties and ice crystal habits of low-level Arctic mixed-phase clouds (MPCs) using *in situ* observations from four aircraft campaigns conducted near Svalbard, Norway. The dataset comprises 45 hours of in-cloud measurements, with 731 600 ice crystal images classified using a convolutional neural network. Observations were categorized into four meteorological regimes using the Marine Cold Air Outbreak index: Marine Cold Air Outbreaks (MCAOs), Warm Air Advections (WAAs), and two transitional states. Vertical profiles of microphysical properties exhibit clear differences between regimes. MCAO conditions are associated with deeper mixed-phase layers, larger ice water contents, and higher concentrations of ice particles. In contrast, WAA cases are associated with shallower clouds dominated by liquid water with lower ice water content. The analysis indicates that temperature inversions influence cloud microphysics: weaker inversions support deeper clouds and enhanced ice development, while stronger inversions limit the extent of the liquid-containing layer. Analysis of ice crystal habits reveals distinct growth patterns based on the meteorological regime and surface type. Rimed particles appear more frequently during MCAOs, particularly over open ocean where increased turbulence likely promotes droplet–ice interactions. Over sea ice, pristine and aggregated crystals are more preva-

https://doi.org/10.5194/egusphere-2026-3265
Preprint. Discussion started: 19 June 2026

lent, implying that riming plays a lesser role while depositional growth and aggregation are more significant. This combined multi-campaign dataset offers a comprehensive statistical view on the interaction of synoptic regime, temperature inversion, and surface conditions in determining the microphysical structure and ice crystal habits of Arctic MPCs.

1 Introduction

The Arctic is undergoing decreasing sea ice and rapid warming, with rates exceeding global warming. These indications of currently observed Arctic climate changes are the result of the action of combined processes and feedback mechanisms specific to the Arctic that amplify the global warming (Wendisch et al., 2023). The multitude of these processes is commonly termed Arctic amplification (Serreze and Francis, 2006). Although the magnitude of this amplification varies seasonally and regionally, recent estimates suggest that Arctic temperatures can increase up to three to four times faster than the global mean (Rantanen et al., 2022). This accelerated warming and the related decrease of extent, thickness, and seasonal persistence of sea ice (Lang et al., 2017; Niederdrenk and Notz, 2018) have led to substantial changes in the surface energy budget (Dong et al., 2010; Shupe et al., 2011). These surface changes reflect the atmospheric feedbacks modifying turbulent heat and moisture fluxes (Boisvert and Stroeve, 2015; Park et al., 2015). In this context, clouds play a role in modulating Arctic amplification, as they influence both atmospheric radiation effects and precipitation processes.

Mixed-phase clouds (MPCs) are ubiquitous in the Arctic (Intrieri et al., 2002; Shupe et al., 2006; Jackson et al., 2012; Wendisch et al., 2019; Cesana et al., 2024) and can persist for several days. In the Svalbard region, low-level MPCs have been reported to occur up to 40 % of the time (Dziduch et al., 2026). MPCs frequently occur as low-level stratiform clouds, particularly as single-layer stratocumulus within the atmospheric boundary layer (McFarquhar et al., 2007). Their vertical structure is characterized by a layer of supercooled liquid water droplets near the cloud top and an underlying layer composed of precipitating or non-precipitating ice crystals (Verlinde et al., 2007; Lloyd et al., 2015; Mioche et al., 2017). However, Arctic MPCs can also occur within multilayer cloud systems, where interactions between vertically separated cloud layers can influence their microphysical structure (Wallentin et al., 2026). The vertical distribution of the microphysical properties controls the cloud optical characteristics, lifetime, and precipitation efficiency (Shupe et al., 2008; Gayet et al., 2009; De Boer et al., 2009; Achtert et al., 2020). Due to their high frequency of occurrence and their specific vertical structure, MPCs play a key role in the Arctic surface radiative budget and hydrological cycle (Kay et al., 2016; McIlhattan et al., 2017). In this context, a detailed characterization of their vertical structure based on *in situ* observations provides important constraints for improving their representation in radiative and hydrological models.

Aircraft measurement campaigns have shown that low-level MPCs typically exhibit cloud top heights below 3 km altitude, which can persist at temperatures up to -30 °C (Shupe et al., 2006; McFarquhar et al., 2007; Gayet et al., 2009). Their microphysical structure is characterized by an increase in liquid water content with height, with maximum values generally near the cloud top. The persistence of MPCs results from a combination of local and mesoscale processes (Morrison et al., 2012; Mioche et al., 2017; Achtert et al., 2020; Chechin et al., 2023; Järvinen et al., 2023). The vertical structure of MPCs is strongly modulated by thermodynamical and dynamical factors, such as boundary-layer stability, cloud–surface coupling (Sotiropoulou

https://doi.org/10.5194/egusphere-2026-3265
Preprint. Discussion started: 19 June 2026

et al., 2014), temperature inversions, vertical wind velocity, and moist-air entrainment driven by cloud-top radiative cooling (Morrison et al., 2012). These processes promote turbulence and vertical circulations that contribute to maintaining the supercooled liquid water phase (Nygård et al., 2014; Pithan et al., 2018). The combined analysis of MPC microphysical properties and thermodynamical conditions provides key insight into how the structure of the atmospheric boundary layer (ABL) controls the partitioning between the liquid and ice thermodynamic phases.

The formation of the ice phase within MPCs is influenced by several factors, including cloud-top temperature, supersaturation, and turbulence (Kanji et al., 2017; Korolev et al., 2017; Chylik et al., 2023). Accurately characterizing the concentration of ice-nucleating particles (INP), which are key drivers of ice crystal formation, and their temporal variability remain essential. However, it is still limited by the scarcity of *in situ* INP observations (Irish et al., 2019; Wex et al., 2019; Hartmann et al., 2021; Rinaldi et al., 2021). In addition, observations of small ice crystals are challenging and subject to significant uncertainties, which hampers the understanding of primary ice production processes. Moreover, secondary ice production (SIP) mechanisms may play a substantial role in explaining observed ice crystal concentrations (Field et al., 2016; Pasquier et al., 2022; Korolev and Lawson, 2026).

Interactions between the liquid water and ice phases in MPCs involve several key microphysical processes, including riming, the Wegener–Bergeron–Findeisen (WBF) process, and aggregation (Pasquier et al., 2022; Järvinen et al., 2023; Korolev and Lawson, 2026). These mechanisms govern both the growth and the habit of ice crystals. In particular, the WBF process promotes the growth of pristine ice crystals through water vapor deposition at the expense of supercooled droplets that are evaporating, while riming leads to the growth of ice particles through the accretion of liquid droplets (McFarquhar et al., 2007; Waitz et al., 2022; Chellini and Kneifel, 2024; Maherndl et al., 2024). Aggregation, in turn, results in more complex and larger structures of ice particles through collisions and sticking between crystals (Chellini et al., 2022; Chellini and Kneifel, 2024). Despite the potential for rapid glaciation driven by the WBF process, the coexistence of these mechanisms contributes to the diversity of observed crystal habits (Mioche and Jourdan, 2018). The classification of the shape of ice crystals and their vertical distribution provides a powerful framework for identifying the dominant microphysical processes and their variability within the cloud.

Although numerous field campaigns have contributed to a better characterization of Arctic MPCs, most observational datasets still have limited geographic coverage and information on surface conditions and thermodynamic regimes. Furthermore, many existing data sets provide sufficient spatial coverage and resolution to characterize the occurrence, concentration, and vertical distribution of hydrometeors, including large ice particles, or detailed *in situ* information on ice particle habits, but rarely both simultaneously (McFarquhar et al., 2007; Mioche et al., 2017). Mioche et al. (2017) examined mean vertical profiles of Arctic MPCs classified by airmass origin, showing how cloud structure and phase partitioning depend on large-scale synoptic conditions, but provided only limited and qualitative information on ice particle habit. More recent studies have further improved the characterization of Arctic cloud microphysics. In particular, Järvinen et al. (2023) analyzed *in situ* microphysical profiles from the Arctic CLoud Observations Using airborne measurements during polar Day (ACLOUD) campaign, focusing on clouds with temperatures between -3.8 °C and -8.7 °C, and proposed a manual classification of ice crystal habit based on Bailey and Hallett (2009). Moser et al. (2023b) described the microphysical properties of Arctic MPCs using observations

https://doi.org/10.5194/egusphere-2026-3265
Preprint. Discussion started: 19 June 2026

from the airborne measurements of radiative and turbulent FLUXes of energy and momentum in the Arctic boundary layer (AFLUX; Mech et al., 2022b) and the MOSAiC Airborne observations in the Central Arctic (MOSAiC-ACA; Mech et al., 2022b) campaign, classifying cloud cases according to the origin of the air mass (open ocean versus sea ice). Building on these efforts, Moser et al. (2025) used observations from the HALO-$(AC)^3$ airborne campaign (HALO, High Altitude and Long Range Research Aircraft – $(AC)^3$ Project on Arctic Amplification Climate Relevant Atmospheric and Surface Processes and Feedback Mechanisms; Wendisch et al., 2024) to quantify differences in microphysical properties between mixed-phase clouds and Arctic low-level mixed-phase haze.

On a larger scale, MPCs are strongly influenced by synoptic conditions, particularly moist warm air intrusions (WAIs) and marine cold air outbreaks (MCAOs) (Kolstad et al., 2009; Fletcher et al., 2016; Chellappan et al., 2024; Wendisch et al., 2024). WAI events are typically associated with the meridional advection of warm, moist air masses and aerosol particles, including particles with the ability to act as INP or cloud condensation nuclei (CCN) (Coopman et al., 2016, 2018; Raif et al., 2024). In contrast, MCAO conditions involve the advection of cold air over relatively warmer surfaces, leading to stronger turbulent heat and moisture fluxes (Brümmer et al., 1992; Papritz and Spengler, 2017; Mroz et al., 2025; Slättberg et al., 2025). As these air masses evolve over sea ice or the open ocean, they affect the aerosol properties, turbulent heat fluxes, and cloud liquid water content (Tjernström et al., 2008; Shupe et al., 2011; Chechin et al., 2023; Moser et al., 2025).

Although recent studies have provided important insights, significant observational challenges remain. In particular, *in situ* measurements of small ice crystals (less than 50 μm in diameter) are still affected by large uncertainties related to sampling limitations and instrument detection thresholds, restricting our ability to fully understand primary and secondary ice formation processes (Jourdan et al., 2010; Wendisch, 2013; Baumgardner et al., 2017; Korolev et al., 2017). In addition, the quantification of INP concentrations remains sparse (Irish et al., 2019; Wex et al., 2019; Raif et al., 2024). These observational limitations are reflected in numerical models, which exhibit a strong sensitivity to microphysical parameterizations and persistent biases in the representation of liquid water and ice phases (Pithan et al., 2014; Hofer et al., 2024). The representation of ice crystal size distributions and habits remains highly simplified and still poorly constrained in atmospheric models, limiting their ability to accurately reproduce observed microphysical processes in MPCs (Tan and Storelvmo, 2019). Current schemes often rely on descriptions of key processes such as ice nucleation, secondary ice production and frequently struggle to capture the co-existence and persistence of supercooled liquid water (Hofer et al., 2024; Raatikainen et al., 2026). As a result, models tend to misrepresent cloud lifetime, vertical structure, and phase partitioning in Arctic MPCs, leading to uncertainties in radiative energy fluxes and precipitation processes (Pithan et al., 2014; Hofer et al., 2024).

Despite recent progress, several key questions remain unresolved. In particular, it remains unclear how large-scale synoptic regimes, such as warm air advections and marine cold air outbreaks, shape the vertical microphysical structure and phase partitioning of Arctic mixed-phase clouds. The extent to which these effects depend on surface conditions, from the open ocean to sea ice, also remains poorly constrained. The role of the boundary-layer thermodynamic structure, especially in temperature inversions, in controlling cloud thickness, liquid partitioning, and ice formation also remains poorly constrained. In addition, the extent to which the habit of ice crystals can be used as an indicator of dominant microphysical growth mechanisms, including riming, depositional growth, and aggregation, remains an open question in contrasting Arctic environments. Addressing these

https://doi.org/10.5194/egusphere-2026-3265
Preprint. Discussion started: 19 June 2026

questions is essential for understanding how coupled dynamical, thermodynamical, and microphysical processes regulate the transition between liquid- and ice-dominated cloud regimes and influence precipitation formation.

To provide an integrated characterization of the microphysical properties and ice crystal morphology of low-level mixed-phase clouds and to assess their dependence upon synoptic meteorological regimes, this study leverages *in situ* observations collected over the Svalbard region during four airborne field campaigns. The Marine Cold Air Outbreak index is used to classify the sampled clouds according to different thermodynamic regimes and to derive mean vertical profiles of their microphysical properties. Particular attention is also given to the influence of temperature inversions on cloud structure and phase partitioning. Finally, ice crystal habits are analyzed under contrasted atmospheric and surface conditions to better identify the processes governing cloud evolution in the Arctic.

2 Data, methods and meteorological settings

2.1 Airborne campaigns

In this study, we analyze and combine the comprehensive *in situ* cloud data collected during four Arctic airborne campaigns, namely ACLOUD, AFLUX, MOSAiC-ACA and HALO-(AC)^3. One of the Alfred Wegener Institute (AWI; Wesche et al., 2016) research aircraft (Polar 5 or Polar 6) was operated to perform remote sensing and *in situ* measurements of aerosol and cloud particles, and precipitation. Dropsondes were also released during the flights to document the vertical thermodynamic structure of the atmosphere. In addition, the High Altitude and Long Range Research Aircraft (HALO) was operated during HALO-(AC)^3. The HALO instrumentation focused on remote sensing observations, and therefore the data collected with HALO instruments during HALO-(AC)^3 were not used in this study. The Polar 5 and Polar 6 aircraft have a range of approximately 2900 km, and their ceiling is around 6 km. The four campaigns took place in the vicinity of Svalbard (Norway); the aircraft were based at Longyearbyen airport. They primarily targeted low-level Arctic clouds, including mixed-phase cloud systems, over regions with contrasting sea ice conditions northwest of Svalbard. Figure 1 shows sea ice concentration (SIC) derived from AMSR2 satellite observations (Spreen et al., 2008), together with flight tracks. SIC was used to characterize surface conditions along the aircraft trajectories.

The ACLOUD campaign (Ehrlich et al., 2019; Wendisch et al., 2019) was conducted in late spring between 23 May and 26 June 2017 and comprised 22 research flights, representing a total of 82.5 hours of measurements. For this study, 17.5 hours of in-cloud observations from the Polar 6 aircraft were analyzed. The AFLUX campaign (Mech et al., 2022a) took place in early spring between 19 March and 11 April 2019. This campaign collected 67 hours of measurements, including 16.3 hours of in-cloud sampling with the Polar 5 aircraft used in this study, distributed among 14 research flights. The MOSAiC-ACA aircraft campaign (Mech et al., 2022a), as part of the Multidisciplinary drifting Observatory for the Study of Arctic Climate (MOSAiC; Shupe et al., 2022) expedition, was held from 30 August to 13 September 2020, with 10 flights. A total of 44 flight hours were conducted, including 7.7 hours of in-cloud sampling performed aboard the Polar 5 aircraft and analyzed here. The HALO-(AC)^3 campaign (Wendisch et al., 2024; Ehrlich et al., 2025) took place between 20 March and 10 April 2022 in early spring. Three research aircraft were involved in this campaign: Polar 5, Polar 6, and HALO. Polar 6 was equipped with *in situ*

https://doi.org/10.5194/egusphere-2026-3265
Preprint. Discussion started: 19 June 2026

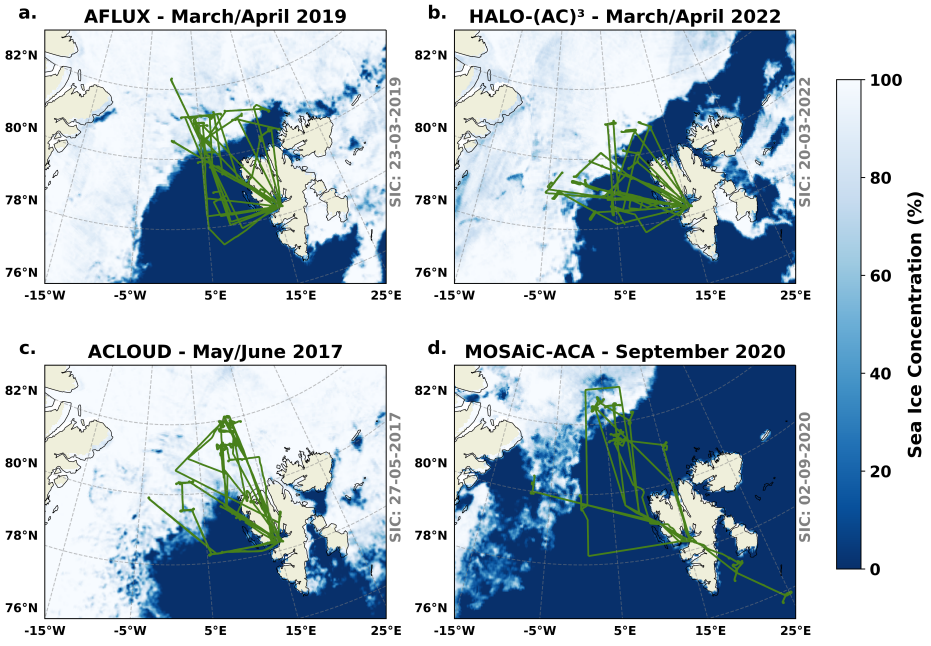

Figure 1. Flight maps for the four aircraft campaigns: **(a)** AFLUX, **(b)** HALO-(AC)^3, **(c)** ACLOUD, and **(d)** MOSAiC-ACA in the vicinity of Svalbard. The colored lines represent flight trajectories for each campaign. The background displays sea ice concentration (SIC) obtained from the Advanced Microwave Scanning Radiometer 2 (AMSR2), with the corresponding SIC date indicated next to each subplot.

measurements and flew for 63 hours, of which 12.2 hours in cloudy conditions are considered in this study, distributed among 13 scientific flights.

Figure 2 shows the Probability Density Function (PDF) of temperature and sea ice concentration along the flight legs, highlighting the contrasting surface environments sampled during each campaign. Three surface regimes were defined based on the SIC values: sea ice for SIC > 80 %, open ocean for SIC < 20 %, and the marginal sea ice zone (MIZ) for intermediate values (20 % to 80 %). AFLUX and HALO-(AC)^3 campaigns were conducted during a similar season and were characterized by relatively cold conditions, with median temperatures of approximately -21 °C and -15 °C, respectively (Fig. 2a). For both campaigns, the majority of the flight time was spent over the open ocean, lasting approximately 22.2 hours for AFLUX and 29.3 hours for HALO-(AC)^3 (Fig. 2b). In contrast, ACLOUD and MOSAiC-ACA were associated with warmer air masses. ACLOUD exhibits a narrow temperature distribution centered around a median of approximately -4 °C. MOSAiC-ACA temperatures have a broader distribution with a median close to -9 °C. Similar to HALO-(AC)^3, MOSAiC-ACA flights were conducted predominantly over the open ocean (more than 26 hours). In contrast, ACLOUD mainly sampled sea ice conditions, with approximately 23.3 hours of flight time over the sea ice.

https://doi.org/10.5194/egusphere-2026-3265
Preprint. Discussion started: 19 June 2026

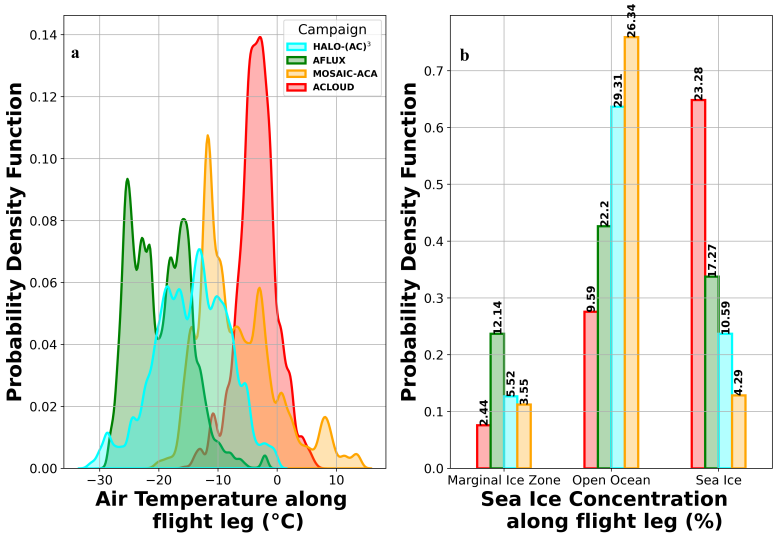

Figure 2. (a) Probability density function of air temperature at aircraft altitude for the four campaigns. **(b)** Distribution of surface types for the four campaigns, classified from sea ice concentration (SIC) into three categories: sea ice (SI; SIC > 80%), open ocean (OO; SIC < 20%), and marginal ice zone (MIZ; 20% < SIC < 80%). Values above each bar indicate the flight time, in hours and minutes, spent over each surface type.

2.2 Meteorological conditions during the campaigns and weather regime classification

Previous studies have highlighted the strong influence of air mass intrusions and transformations on mixed-phase cloud properties in the Arctic (Michaelis et al., 2022; Wendisch et al., 2025; Mroz et al., 2025; Dziduch et al., 2026). The MCAO index represents the combined effect of cold air advection and air-sea interaction (Fletcher et al., 2016). The MCAO index is calculated from six-hourly fifth-generation ECMWF reanalysis data (ERA5) (Hersbach et al., 2020) as the potential temperature difference between the surface and the 850 hPa air pressure level (Kolstad et al., 2009). The MCAO index is computed only over ice-free ocean grid points and averaged over the eastern Greenland Sea, defined here as the region between 75.00–80.25 °N and 4.50–10.50 °E (Knudsen et al., 2018). Therefore, the MCAO index provides an estimate of the lower-tropospheric thermodynamic stability over open ocean, with positive values indicating cold air advected over a relatively warm surface and enhanced boundary-layer instability, while negative values correspond to stable conditions with warm air above cold surface.

This relationship is further supported by a complementary principal component analysis (see Table S1, Figure S1-S2, and Text S1 in the Supplement), which reveals that the MCAO index plays a key role in the cloud thermodynamic phase partitioning. We therefore use the MCAO index to segregate key atmospheric conditions and investigate the influence of large-scale meteorological regimes on cloud characteristics.

An MCAO event is defined as a period of at least 48 consecutive hours during which the MCAO index remains positive (MCAO > 0 K) and exceeds a threshold value within this period. This threshold is set to 2 K during the warm season (ACLOUD

https://doi.org/10.5194/egusphere-2026-3265
Preprint. Discussion started: 19 June 2026

and MOSAiC-ACA), when MCAO events are generally weaker, and to 3 K during the cold season (AFLUX and HALO-(AC)^3), consistent with previous studies (Kolstad et al., 2009; Fletcher et al., 2016; Knudsen et al., 2018). Warm Air Advection (WAA) events are also identified based on pronounced negative anomalies of the MCAO index. Specifically, a WAA event is defined when the MCAO index is at least 10 K lower than the 1979–2022 climatological mean (Tjernström et al., 2014; Knudsen et al., 2018). Once this threshold is exceeded, the same temporal criteria as for MCAO events are applied. In addition to MCAO and WAA events, two transitional regimes are defined: Norm-C, corresponding to a moderately negative index (MCAO index > –2.5 K) that does not qualify as MCAO, and Norm-W, defined by a negative index (MCAO index < –2.5 K) that does not exceed the WAA threshold. The temporal evolution of the MCAO index during the four airborne Arctic campaigns is presented in Figure 3.

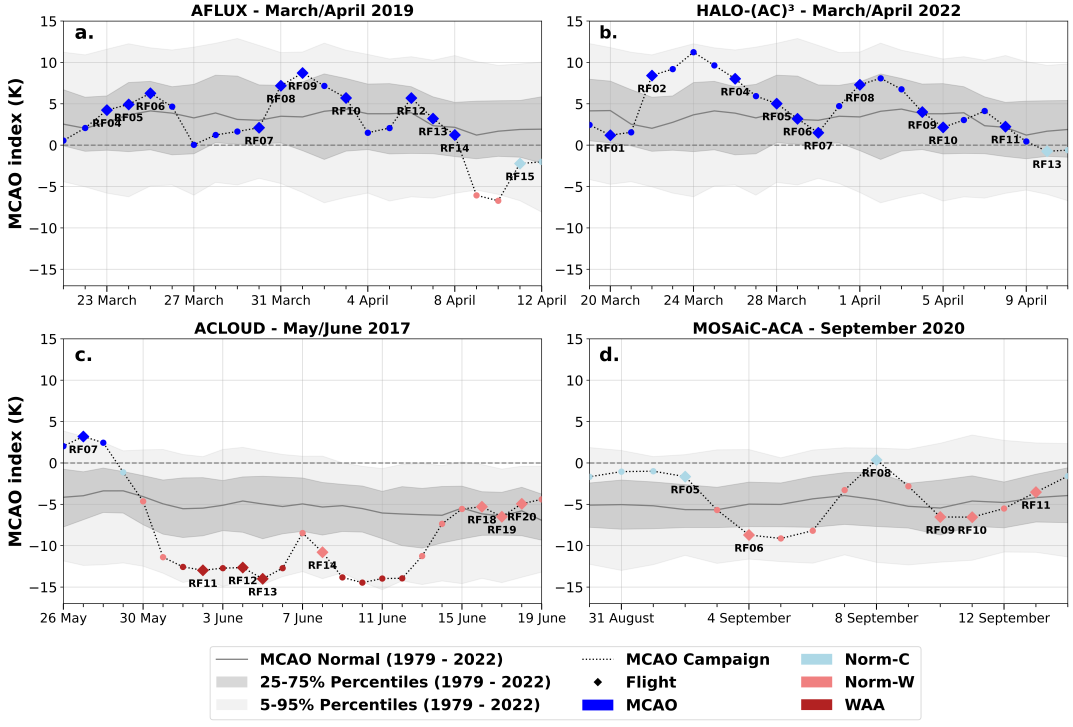

Figure 3. Daily evolution of the MCAO index (dotted lines) during the airborne campaigns **(a)** AFLUX (March–April 2019), **(b)** HALO-(AC)^3 (March–April 2022), **(c)** ACLOUD (May–June 2017), and **(d)** MOSAiC-ACA (September 2020). The Marine Cold Air Outbreak (MCAO) index is plotted relative to the ERA5 climatology (1979–2022) in straight lines, with shaded areas indicating the 25th–75th (dark shading) and 5th–95th (light shading) percentile ranges. Colors denote individual flight days, classified by regime: Marine Cold Air Outbreak (MCAO: dark blue), Normal-Cold (Norm-C: light blue), Normal-Warm (Norm-W: light red), and Warm Air Advection (WAA: dark red).

The ACLOUD (Fig. 3c) and MOSAiC-ACA (Fig. 3d) campaigns were characterized by predominantly low or negative MCAO index. During ACLOUD, the MCAO index remained close to or below 0 K for most of the period, with only a brief MCAO phase at the beginning of the campaign, followed by extended WAA conditions (Knudsen et al., 2018). Similarly, during

https://doi.org/10.5194/egusphere-2026-3265
Preprint. Discussion started: 19 June 2026

MOSAiC-ACA, the MCAO index varied between 0 K and -8 K throughout the campaign, indicative of weak thermodynamic forcing and limited instability (Kolstad et al., 2009; Papritz and Spengler, 2017). In contrast, the AFLUX (Fig. 3a) and HALO-(AC)^3 (Fig. 3b) campaigns were marked by pronounced MCAO conditions. AFLUX featured multiple strong MCAO episodes, with MCAO index values exceeding 5 K for several days between late March and early April. Similarly, HALO-(AC)^3 exhibited long periods of strong MCAO as characterized in detail by Walbröl et al. (2024), while neutral conditions characterized the end of the campaign.

The mean temperature profiles measured by the dropsondes, along with the associated temperature inversions, are presented in Figure 4 for the different regimes. MCAO cases are characterized by a colder lower troposphere, with temperatures ranging from approximately –14 °C near the surface to –20 °C at 700 hPa. The temperature profiles analyzed indicate that, on average, MCAO conditions are associated with weaker and/or less vertically extensive temperature inversions than WAA conditions. However, individual MCAO cases still frequently exhibit a marked capping inversion at the top of the boundary layer. Individual profiles exhibit a well-mixed and unstable boundary layer over the ocean, consistent with the development of shallow convective structures.

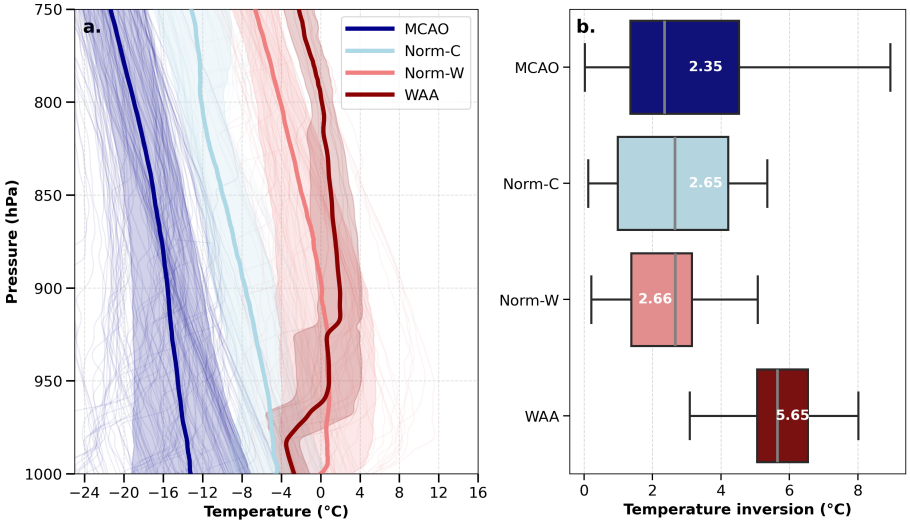

Figure 4. (a) Mean vertical profiles of air temperature (°C) derived from dropsonde observations for the different regimes: MCAO, Norm-C, Norm-W, and WAA. Thin lines represent individual profiles, while thick lines indicate regime-mean profiles for all surface types; shaded areas correspond to standard deviation. **(b)** Boxplots showing the distribution of temperature inversion (°C) between cloud base and cloud top for each regime from aircraft observations. Boxes represent the interquartile range and horizontal lines indicate the median. The corresponding median values are shown in each box.

In contrast, WAA regimes exhibit a significantly different vertical thermodynamic structure. Pronounced low-level temperature inversions are visible in Figure 4a. Temperatures increase from –4 °C in the lowest layers to around 2 °C near 900 hPa. On average, aircraft temperature profiles reveal an inversion strength of approximately 5.6 °C between the cloud base and the

https://doi.org/10.5194/egusphere-2026-3265
Preprint. Discussion started: 19 June 2026

cloud top, reflecting enhanced stability in the lower troposphere. Transitional regimes (Norm-C and Norm-W) display intermediate characteristics between these two extremes. Although Norm-C remains overall colder than Norm-W, both regimes show notable differences in their thermodynamic profiles. However, their temperature inversions are relatively similar, with median values around 2.7 °C. The median temperature inversions derived for the MCAO and WAA regimes are used to investigate the influence of temperature inversions on the microphysical profiles. Additional analysis shows that the local temperature inversion calculated between cloud base and cloud top is accurately represented by the Estimated Inversion Strength (EIS, Wood and Bretherton, 2006), despite EIS being more representative of larger-scale conditions.

2.3 Airborne instrumentation for *in situ* observations

The *in situ* cloud measurement payload remained similar across all four campaigns. The following section provides a list of all instruments used for the analysis of mixed-phase cloud microphysical properties. Table 1 lists the instruments used in the respective campaigns.

The Cloud Imaging Probe (CIP, Baumgardner et al., 2001), Precipitation Imaging Probe (PIP, Baumgardner et al., 2001) and the Two-Dimensional Stereo spectrometer (2D-S, Lawson et al., 2006) are optical array probes (OAPs) that measure the size and the shape of hydrometeors (cloud particles, drizzle, rain, and ice particles). They also provide a quantitative dataset of hydrometeor images. The sampling volume is computed for each image, which allows for computation of cloud particle concentrations. The cloud particles are then distributed into size bins according to the instrument resolution to produce a Particle Size Distribution (PSD). Two types of CIP are used, depending on the campaign, both composed of 64 photodiodes: one with a resolution of 15 μm, covering a size range from 15 μm to 960 μm, and another with a resolution of 25 μm, covering a size range from 25 μm to 1600 μm. The 2D-S has a resolution of 10 μm with 128 bins ranging from 10 μm to 1280 μm. The PIP has 64 photodiodes with a resolution of 100 μm corresponding to a nominal size range of 100–6400 μm. For particles smaller than 100 μm, uncertainties in number concentration range from 50 % to 100 %. Moreover, for particles larger than 100 μm, uncertainties are around 20 % for particle sizing and 50 % for number concentration (Baumgardner et al., 2017).

Table 1. Instrument status for each campaign. A checked box indicates that the instrument was used.

Instrument	ACLOUD	AFLUX	MOSAiC-ACA	HALO-(AC)^3
CDP	☒		☒	☒
CAS		☒		
SID-3	☒			
2D-S		☒	☒	☒
CIP	☒			
PIP	☒	☒	☒	☒
PN		☒	☒	☒

https://doi.org/10.5194/egusphere-2026-3265
Preprint. Discussion started: 19 June 2026

Two size spectrometers were also available, the Cloud Droplet Probe (CDP, Lance et al., 2010) and the Cloud and Aerosol Spectrometer (CAS, Baumgardner et al., 2001). Both are forward-scattering spectrometers, in which light scattered by particles crossing their laser beam is detected within a range of angles between 4° and 12°. The signal is then processed to retain only in-focus particles and to determine their size. Their measurement ranges are 2 μm to 50 μm and 0.5 μm to 50 μm for the CDP and CAS, respectively. The CDP size distribution was recorded over 30 size bins, while the CAS initially provided 30 size bins, which were reduced to 11 bins after applying the Mie binning approach (Mech et al., 2022a). For ACLOUD research flights 07 to 15, the CDP was not operational, and small cloud particles were measured using the Small Ice Detector Mark 3 (SID-3, Hirst et al., 2001). The SID-3 measures individual cloud particles by recording two-dimensional patterns of forward scattering light over angles from 5° to 26°. It covers a size range from 5 μm to 45 μm, divided into 16 size bins with a size resolution between 2 μm and 5 μm. Related uncertainties are at most 50 % for sizing and 20 % for number concentration. Both instruments, as well as for all OAPs, were equipped with anti-shattering tips.

The Polar Nephelometer (PN, Gayet et al., 1997) collects the angular scattering intensities (non-normalized scattering phase function) of a volume of particles on a circular photodiode array. The angular range of the PN extends from 4.28° to 169°. Only measurements from 15° to 169° are selected to avoid the light contamination from the laser at the smallest angles. The asymmetry parameter (g) is calculated following Gerber et al. (2000), and the derivation of extinction from the non-normalized scattering phase function is presented in Gayet et al. (2002). The uncertainties associated with the derived parameters are documented in Jourdan et al. (2010). The average uncertainty in angular scattering coefficient (ASC) measurements ranges from 3 % to 5 %, depending on the scattering angle, while the extinction coefficient uncertainty is on the order of 25 %.

In addition to these cloud probes, several *in situ* aerosol probes were operated onboard the aircraft. The Ultra-High-Sensitivity Aerosol Spectrometer (UHSAS, Cai et al., 2008) measured aerosol number size distributions typically between 60 nm and 1000 nm. The Condensation Particle Counter (CPC, Mertes et al., 1995) detected the total number concentration of particles larger than 10 nm. Both instruments were installed downstream of the Counterflow Virtual Impactor (CVI, Mertes et al., 2019), which enables the selective sampling of cloud residual particles by separating interstitial aerosols from evaporated cloud hydrometeors. This setup provided complementary information on ambient aerosol properties.

2.4 Processing microphysical data

Data processing is conducted in two steps for all probes used in each campaign. First, a raw PSD is extracted from the CDP or CAS data using the software PADS (Particle Analysis and Display System) provided by DMT (Droplet Measurement Technologies). Then, the sampling volume is corrected using the true air speed of the aircraft and the sampling area associated with each probe. For OAPs (CIP, 2D-S, and PIP), datasets of particle images and geometric features are extracted and processed following Leroy et al. (2016), from which the PSD is computed. Contamination from splashing and shattering caused by collisions of ice and liquid water particles on probe inlets is identified and removed according to inter-arrival time statistics (Korolev et al., 2011).

All OAP images are classified using a Convolutional Neural Network (CNN, Jaffeux et al., 2022). The CNN model was primarily trained using images from HAIC-HIWC (High Altitude Ice Crystals–High Ice Water Content), EXAEDRE (EX-

https://doi.org/10.5194/egusphere-2026-3265
Preprint. Discussion started: 19 June 2026

ploiting new Atmospheric Electricity Data for Research and the Environment), and EUREC^{4}A (Elucidating the role of clouds-circulation coupling in climate), with additional Arctic data from AFLUX (Dezitter et al., 2013; Defer et al., 2015; Bony et al., 2022; Jaffeux et al., 2022). To improve the consistency and performance of the CNN, we manually classified approximately 900 cloud particle images extracted from the four Arctic campaigns for each of the eight model classes (see Jaffeux et al. (2022) for more details). Then, these images were included in the training dataset of the model. The morphological classes and their associated dominant growth process are illustrated in Figure 5. Only particle images larger than 300 μm for the 2D-S, 450 μm for the CIP, and 2000 μm for the PIP can be classified by the model (corresponding to images with at least 20 pixels). A total of 731,600 particle images were classified by the CNN throughout the four analyzed campaigns, providing a robust statistical basis for investigating ice crystal habit and its variability under different environmental conditions. Another outcome of the processing chain is to improve the segregation between the liquid water droplets and the ice crystals. The circularity parameter, as defined by Crosier et al. (2011), is calculated and used to separate the PSD of spherical particles (considered as liquid) from the PSD of non-spherical particles (considered as ice).

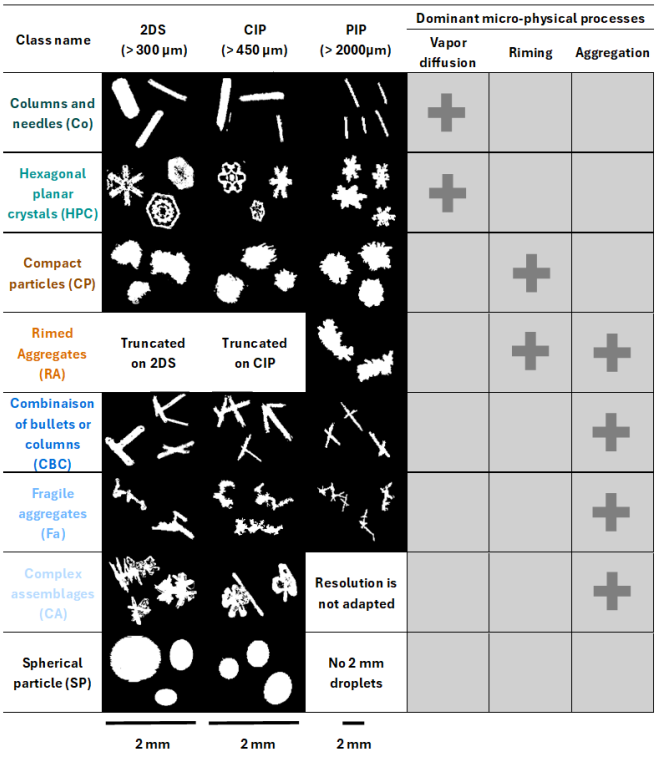

Figure 5. Morphological classification of hydrometeors identified by the convolutional neural network (CNN) adapted from Jaffeux et al. (2022) and Bazantay et al. (2025). The eight morphological classes are shown as observed by the three imaging probes: 2D-S (> 300 μm), CIP (> 450 μm), and PIP (> 2000 μm). Dominant microphysical processes associated with each class (vapor diffusion, riming, and aggregation) are indicated in the rightmost panel.

https://doi.org/10.5194/egusphere-2026-3265
Preprint. Discussion started: 19 June 2026

In this study, *in situ* data processing follows the general methodology developed by Raillard et al. (2024). The key difference concerns the upper bound of the liquid PSD. Raillard et al. (2024) extended the liquid PSD to 500 μm to account for precipitating droplets within the melting layer. In contrast, for the colder conditions sampled in the AFLUX and HALO-(AC)^3 campaigns, this upper threshold was reduced to 300 μm. This choice prevents large, spherical graupel particles from being misclassified as liquid water drizzle. Consistently, no evidence of rain or radar signatures associated with a melting layer was observed in our dataset. The complete processing algorithm is described in Figure S3 of the Supplement.

The presence of drizzle around 300 μm is consistent with observations of drizzle particles during ACLOUD (Järvinen et al., 2023) or during the Ny-Ålesund Aerosol Cloud Experiment (NASCENT) campaigns (Pasquier et al., 2022). Below 50 μm, the probes cannot reliably discriminate the particle phase. Therefore, all particles smaller than this limit are considered to consist of liquid water (McFarquhar et al., 2007; Korolev et al., 2017). To ensure consistency in the retrieval of phase partitioning, we also tested the phase discrimination criteria proposed by D'Alessandro et al. (2019) on the CDP measurements. The results show agreement with the phase partitioning derived from particle circularity, confirming the robustness of our segregating method. In contrast to the mid-latitude conditions reported by D'Alessandro et al. (2019), the CDP identified only a very small fraction of ice or aerosol particles in the Arctic datasets. This is consistent with the prevalence of supercooled liquid water droplets observed at small size bins.

Figure 6 presents an example of the merged PSD combining the CAS, 2D-S, and PIP measurements collected during AFLUX research flight 12. The overlapping size ranges of the instruments are treated as follows: in the lower size range of the distribution, the CDP/CAS is used up to a maximum size of 33 μm. A weighted mean between CDP/CAS and 2D-S/CIP is computed over the size range 33–43 μm, with bins of the 2D-S/CIP resized using interpolation. The CIP/2D-S is then used from 50 μm up to the threshold (300 or 500 μm), depending on the conditions described above. Subsequently, a weighted mean between the CIP/2D-S and PIP is computed from one of these thresholds up to 1,280 μm, after resizing the PIP bins by interpolation to match the CIP/2D-S bin size over the overlapping range. Above this threshold, only the PIP is used to compute the merged PSD.

The microphysical parameters associated with each phase (ice and liquid) are then derived, including the total particle number concentration (N), the effective diameter (D_{eff}), the extinction coefficient (σ), and the water content (LWC for liquid or IWC for ice). For the ice phase, number concentration was calculated by considering non-spherical particles larger than 50 μm. All microphysical parameters are computed following the same methodology as described in Mioche et al. (2017) and Järvinen et al. (2023). The IWC is computed using a mass–dimension relationship of the following form:

$$m = a \cdot D^b, \tag{1}$$

where D is the maximum particle diameter in meters, m is the crystal's mass in kg with a = 0.0121 kg m^{-b}, and b = 1.9, following a modified version of Brown and Francis (1995) proposed by Hogan et al. (2012). The calculation of IWC is highly sensitive to the choice of the mass–diameter (M-D) relationship. This relationship depends on assumptions on particle habit and density. Significant variability in IWC is observed when different parameterizations are applied. In our analysis of a dataset comprising 876,908 particles ranging from 300 μm to 3,184 μm, the Brown and Francis (1995) relationship (modified by

https://doi.org/10.5194/egusphere-2026-3265
Preprint. Discussion started: 19 June 2026

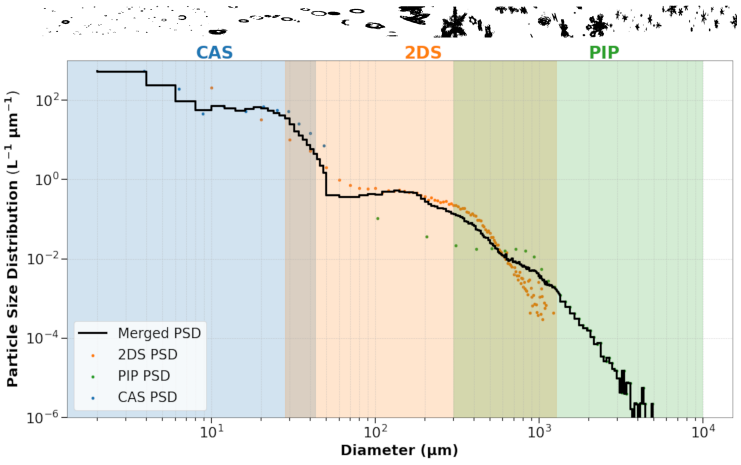

Figure 6. Mean PSD for each instrument during AFLUX flight 12 (06 April 2019) and the resulting merged PSD in black. Images sampled by the differents OAPs are presented above the plot for different cloud phases. The shaded areas indicate which instrument the particles were sampled from.

Hogan et al., 2012) systematically yields higher IWC values than the method proposed by Baker and Lawson (2006), with differences strongly dependent on the particle habit. Järvinen et al. (2023) indicate that alternative M-D law can reduce IWC estimates by 40–60 % when using the McFarquhar et al. (2007) relationship, and by up to 85 % for specific types of ice crystals such as needles or rimed particles, compared to Brown and Francis (1995). Our results further confirm pronounced habit-dependent biases, including an overestimation that exceeds 100 % for columnar particles when using Brown and Francis (1995) method instead that of Baker and Lawson (2006). These findings highlight that the choice of M-D relationship remains a major source of uncertainty in IWC retrievals, particularly in mixed-phase clouds where habit variability is large. A more detailed comparison of IWC estimates derived from different M-D relationships is provided in the Supplement (Table S2 and Text S2).

Moreover, a theoretical adiabatic LWC (LWC_{adiab}) is calculated and compared to observations. The liquid water ratio is defined as the ratio between the *in situ* LWC and the adiabatic LWC (LWC_{adiab}). The latter is estimated assuming a non-entraining moist air parcel rising from cloud-liquid base to cloud-liquid top and reaching saturation. It is calculated from pressure and temperature measurements along the profile (Mioche et al., 2017; Järvinen et al., 2023).

2.5 Atmospheric measurements and turbulence parameters

A combination of *in situ* aircraft measurements and dropsonde profile data is used to characterize the thermodynamic and dynamic airmasses in which the low-level Arctic clouds evolve. The aircraft (Polar 5 and Polar 6) were equipped with the same noseboom-mounted meteorological instrument package designed to measure airflow and thermodynamic variables with high temporal resolution required to derive turbulent fluxes. Air motion was derived from Rosemount 858 multi-hole probes, while

https://doi.org/10.5194/egusphere-2026-3265
Preprint. Discussion started: 19 June 2026

air temperature was measured using fast-response open-wire Pt100 sensors. These fast sensors were complemented by slower-response Vaisala HMT-333 instruments providing air temperature and humidity, together with static pressure measurements. Meteorological variables, including pressure, three-dimensional wind vector components, air temperature, and humidity, were recorded at high temporal resolution (100 Hz) but are also available at 1 Hz through temporal averaging (Hartmann et al., 2018). Dropsondes (Ehrlich et al., 2019; Mech et al., 2022a; George et al., 2024) were deployed to obtain high-resolution vertical profiles of temperature, humidity, pressure, and horizontal wind from flight altitude to the surface.

Turbulence properties are derived following the methodology of Chechin et al. (2023), using the high-frequency (100 Hz) measurements. Only horizontal legs and vertical profiles with low ascent and descent rates ($\approx$ 0.5–1.5 m s^{-1}) are considered. Turbulence parameters are computed using a moving window of 100 s, corresponding to a flight distance of approximately 5–10 km (for aircraft speeds about 50 m s^{-1}). This window length is chosen to separate the mesoscale variability from turbulent fluctuations. Slanted profiles provide quasi-continuous information on the vertical structure but are associated with increased statistical uncertainty and vertical smoothing. The quantities analyzed include the variances of the velocity turbulent fluctuations (u'^2, v'^2, w'^2), the turbulent kinetic energy (TKE), and the vertical sensible heat flux (H), defined as:

$$TKE = \frac{1}{2}(u'^2 + v'^2 + w'^2) \tag{2}$$

$$H = \rho\, c_\mathrm{p}\, \overline{w'\theta'} \tag{3}$$

where ρ is the air density, c_p is the specific heat capacity of air, and θ' denotes the fluctuation of the dry air potential temperature. For details on measurement uncertainties, we refer to Hartmann et al. (2018), while additional information on the derivation of turbulence parameters is provided in Appendix A of Chechin et al. (2023).

2.6 Profile selection and normalized altitudes

This study is based on a set of 35 *in situ* flights conducted during four campaigns in the Arctic region covering a wide range of meteorological and thermodynamical conditions. Most of the sampled clouds were low-level clouds with top heights located below 2 km altitude. To enable consistent intercomparison of cloud vertical profiles representative of various cloud and thermodynamic structures, cloud altitudes are normalized based on equations 4 and 5 following the method described by Jackson et al. (2012) and applied by Mioche et al. (2017), Chechin et al. (2023) and Järvinen et al. (2023):

$$Z_\mathrm{n} = \frac{Z - Z_\mathrm{b}}{Z_\mathrm{t} - Z_\mathrm{b}} \quad \text{for } Z_\mathrm{b} < Z < Z_\mathrm{t} \tag{4}$$

$$Z_n = \frac{Z}{Z_\mathrm{b}} - 1 \quad \text{for } Z < Z_\mathrm{b}, \tag{5}$$

where Z is the altitude of the aircraft, and Z_t and Z_b correspond to the top and base of the liquid cloud layer, respectively. A normalized value of 1 corresponds to the top of the liquid-containing cloud layer, while Z_n = 0 marks its base. Negative

https://doi.org/10.5194/egusphere-2026-3265
Preprint. Discussion started: 19 June 2026

values indicate the underlying ice layer, with Z_n = -1 representing the lowest sampled level. Figure 7 illustrates the method used to identify the top and the base of the cloud from the aircraft observations. Variations in LWC (LWC > 0.01 g m^{-3}) and in the asymmetry parameter g serve as primary diagnostics: values of g > 0.83 indicate a predominantly liquid water phase, while lower values (g < 0.80) show ice conditions (Mioche et al., 2017; Mioche and Jourdan, 2018). When available, radar reflectivity (Fig. 7b) and lidar backscattering data (not shown) are used to confirm or refine the phase boundaries (especially for cloud-top). This approach is used to determine the base and top of the liquid layer and to derive normalized vertical profiles of microphysical properties (Fig. 7e-f). All cloud properties presented in this study are computed within cloud regions where the LWC exceeds 0.01 g m^{-3} or the ice extinction coefficient (σ_i) exceeds 0.05 km^{-1}.

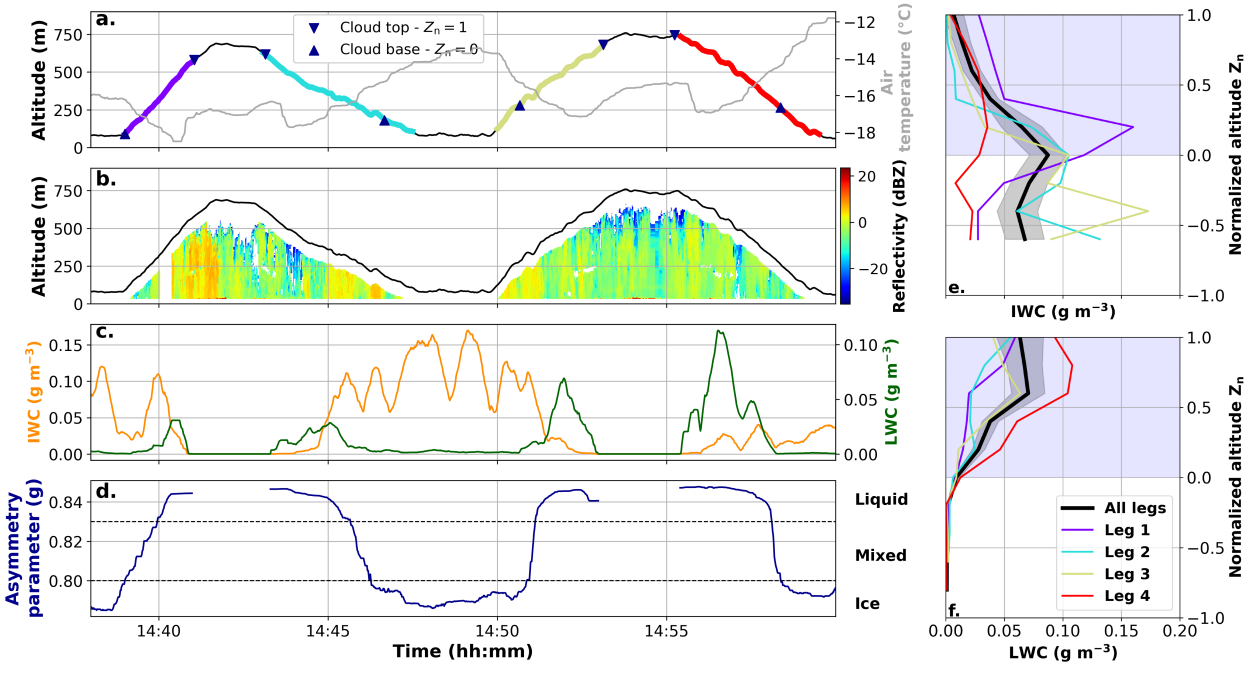

Figure 7. *In situ* cloud measurements during the sawtooth pattern of Flight 06 (25 March 2019, AFLUX). (**a**) Aircraft altitude (black) and air temperature (grey); cloud tops and bases are marked by triangles with Z_n = 1 (liquid top) and Z_n = 0 (liquid base). (**b**) Radar reflectivity from MiRAC-A with flight altitude overlaid in black (blindzone). (**c**) Ice (orange) and liquid (green) water contents (g m^{-3}). (**d**) Asymmetry parameter g (dark blue); phase thresholds: g > 0.83 (liquid), g < 0.80 (ice), 0.83 > g > 0.80 (mixed-phase). (**e**–**f**) Median vertical profiles of LWC and IWC.

This methodology is applied to 430 flight segments (including both horizontal and vertical legs), representing more than 45 hours of in-cloud measurements. The macrophysical cloud properties for the four campaigns are presented in Supplement Table S3. The microphysical profiles presented in the results section are expressed as median values with the 99 % confidence interval of the median. Normalized vertical profiles are constructed using bins ranging from -1.0 to 1.0 with a step of 0.2. This

https://doi.org/10.5194/egusphere-2026-3265
Preprint. Discussion started: 19 June 2026

approach aims to represent a typical (median) microphysical structure, bearing in mind that horizontal sampling introduces substantial variability and contributes to a large spread in the data.

3 Microphysical profiles

3.1 Microphysical properties based on MCAO regime

The vertical cloud microphysical structure of MPCs is investigated for the four contrasting weather regimes (WAA, Norm-W, Norm-C, and MCAO) identified in section 2.2. The objective is to document how phase partitioning responds to variations of large-scale thermodynamic conditions and to assess how these conditions influence the cloud microphysical and macrophysical properties. The statistics of the cloud macrophysical characteristics for each category are summarized in Table 2. The vertical variability of liquid and ice microphysical properties is examined using normalized altitude profiles (Fig. 8).

Table 2. Macrophysical properties of clouds sampled under different MCAO weather regimes. Values include the number of sampling legs (N_{leg}), in-cloud measurement time (t_{cld}), and the base (Z_{b}), top (Z_{t}), and thickness (H_{cld}) of the liquid-containing cloud layer, as well as the cloud-top temperature (T_{top}). Median values are shown with interquartile ranges in brackets.

MCAO Regime	N_{leg}	t_{cld} (min)	Z_{b} (m)	Z_{t} (m)	H_{cld} (m)	T_{top} (°C)
MCAO	257	1527	290 [100/500]	620 [400/910]	320 [170/460]	-16.5 [-18.5/-14.7]
Norm-C	40	199	185 [60/223]	670 [398/1610]	465 [198/925]	-11.1 [-13.2/-6.8]
Norm-W	89	584	90 [50/400]	620 [470/1160]	420 [330/660]	-3.6 [-6.1/-1.8]
WAA	44	417	173 [90/236]	440 [105/538]	265 [240/340]	-3.3 [-5.1/-1.8]

The results show that MPCs influenced by WAA exhibit a vertical structure dominated by the liquid phase and capped by a strong temperature inversion near the cloud top (Fig. 4b). The droplet number concentration and effective diameter continuously increase from the cloud base to the upper part of the cloud, with maximum values of approximately 125 cm^{-3} for N_{w} at $Z_{\mathrm{n}} \approx 0.75$ and $D_{\mathrm{eff,w}}$ exceeding 20 μm at the cloud top (Z_{n} = 1). Accordingly, the LWC and the extinction coefficient increase sharply towards the cloud top, with maxima above 0.45 g m^{-3} and 65 km^{-1} observed at $Z_{\mathrm{n}} \approx 0.75$ (Fig. 8c, d). Complementary information is provided in Figure 9, which shows normalized profiles of the liquid water ratio (*in situ* to adiabatic liquid water content), relative humidity, and vertical velocity variance. In the liquid-containing layers (Z_{n} between 0 and 1), the ratio of LWC to LWC$_{adiab}$ remains close to 1, and the increase in LWC and droplet size is consistent with adiabatic cooling in cloud-scale updrafts (Fig. 9, red curve). Macrophysical statistics (Table 2) show that WAA clouds are relatively shallow, with a median thickness of about 265 m and cloud-top altitudes near 440 m. This vertical structure is consistent with the profile of vertical velocity variance (w'^2, Fig. 9c), suggesting that enhanced turbulence below the cloud may contribute to a supply of moisture from lower levels. Additional moisture sustaining the liquid phase may also be provided by the large-scale advection of water vapor associated with low-level jets, which frequently occur during WAA (Chechin et al., 2023; Järvinen et al., 2023).

https://doi.org/10.5194/egusphere-2026-3265
Preprint. Discussion started: 19 June 2026

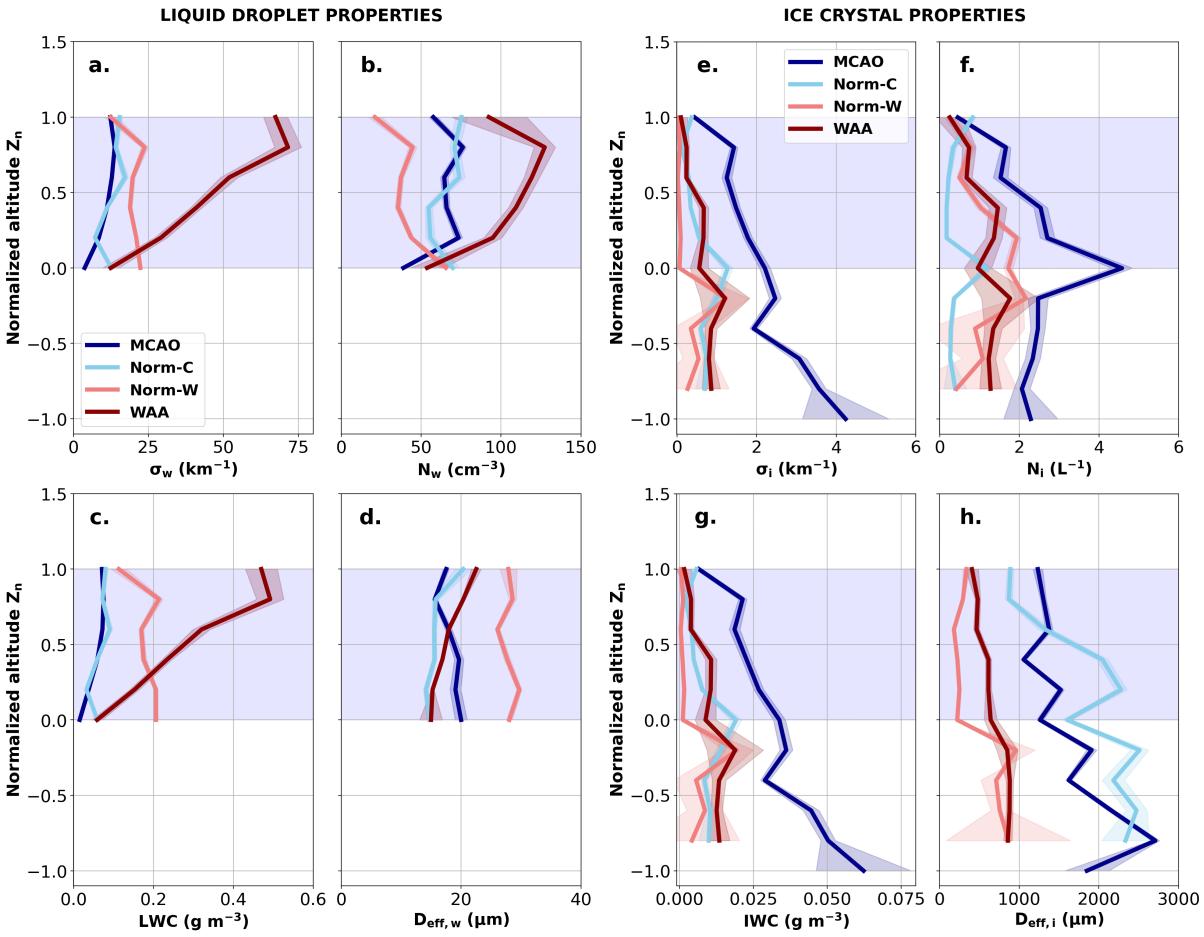

Figure 8. Normalized vertical profiles of cloud microphysical properties for four thermodynamic regimes: MCAO (dark blue), Norm-C (light blue), Norm-W (light coral), and WAA (dark red). Liquid droplet properties: (**a**) extinction coefficient (σ_{w}), (**b**) droplet number concentration (N_{w}), (**c**) liquid water content (LWC), and (**d**) droplet effective diameter ($D_{\mathrm{eff,w}}$). Ice crystal properties: (**e**) extinction coefficient (σ_{i}), (**f**) ice crystal number concentration (N_{i}) larger than 50 μm, (**g**) ice water content (IWC), and (**h**) ice particle effective diameter ($D_{\mathrm{eff,i}}$). The large shaded area between Z_n = 0 and Z_n = 1 represents the vertical extent of the liquid-layer cloud. Lines represent the median across profiles for each regime, and shaded envelopes indicate the 99 % confidence interval of the median.

In the uppermost cloud layers ($Z_{\mathrm{n}} > 0.8$), the number and mass concentrations decrease, while the droplet size continues to increase until the cloud top is reached. Figure 9a shows that the LWC profile becomes sub-adiabatic in these layers. This may result from the entrainment of warm and dry air from above, leading to partial evaporation of the smallest water droplets and thus an increase in the median $D_{\mathrm{eff,l}}$. Droplet–ice interaction mechanisms such as the WBF process or riming may also contribute to the decrease in droplet concentrations. Figure 8e–h displays the vertical profiles of ice crystal properties. In MPCs influenced by WAAs, the number concentration of ice crystals is typically below 2 L^{-1} throughout the cloud layers. The

https://doi.org/10.5194/egusphere-2026-3265
Preprint. Discussion started: 19 June 2026

effective dimensions of ice crystals are smaller near cloud top ($D_{\mathrm{eff,i}} < 500$ μm), but increase gradually toward the cloud base, reaching 800–900 μm in the ice layers ($Z_{\mathrm{n}} < 0$). The ice crystal number concentration (for particles larger than 50 μm) peaks at mid-level within the mixed-phase layer ($Z_{\mathrm{n}} \approx 0.5$). This pattern indicates that ice formation likely occurs near the cloud top where the temperature inversion is stronger and radiative cooling is more pronounced. Accordingly, Järvinen et al. (2023) showed during ACLOUD that SID-3 measurements reveal high concentrations of small ice crystals (< 50 μm) near cloud top, reaching up to 18 L^{-1}. However, ice crystals require time to grow to detectable sizes as they sediment. This may be a reason why the maximum concentration of ice crystals is observed in lower cloud layers.

Norm-W regimes are characterized by warm thermodynamic conditions (Fig. 4a), with cloud-top temperatures comparable to those observed in WAAs (-3.6 °C, Tab. 2), but capped by a much weaker temperature inversion (Fig. 4b). The liquid phase remains relatively pronounced, with LWC values around 0.17-0.20 g m^{-3} and $D_{\mathrm{eff,w}}$ close to 25-30 μm, and fairly evenly distributed throughout the vertical layers of the cloud (Fig. 8c–d). The liquid layer is thicker, with a median depth of about 420 m and tops reaching approximately 620 m. The adiabatic ratio profile in Norm-W clouds is among the most variable across all regimes (Fig. 9a). It starts near 0.8 at the base of the liquid layer and decreases sharply with increasing altitudes to values as low as 0.4 near the cloud top, pointing to a strongly sub-adiabatic structure. The relatively high values at cloud base, along with the increase in w'^2 below the cloud, suggest a localized moisture supply from below. This moisture input appears to be consumed in the lower part of the liquid layer, contributing to the observed sub-adiabatic profiles aloft. As shown in Figure 8e-h, ice-phase concentrations are variable and generally low: IWC reaches only 0.02 g m^{-3} in the ice part of the cloud ($Z_{\mathrm{n}} < 0$), and the number concentration peaks near 2 L^{-1}. A marked change in effective size is also observed along the vertical profile, with values below 500 μm in the upper cloud layers ($Z_{\mathrm{n}} > 0$) and close to 1000 μm in the lower part of the profile ($Z_{\mathrm{n}} < 0$). The observed increase in crystal size is more consistent with growth occurring gradually within the mixed-phase layer, followed by sedimentation toward lower levels. As crystals fall, larger particles dominate, leading to an increase in effective diameter ($D_{\mathrm{eff,i}}$) and a decrease in number concentration.

Compared to Norm-W cases, Norm-C regimes occur in a colder environment. In these clouds, the median cloud-top temperature is -11.1 °C (Tab. 2). Relative humidity with respect to water (Fig. 9b) remains close to saturation throughout the mixed cloud layer, while ice supersaturated conditions are maintained. A slight decrease of $\mathrm{RH_{ice}}$ is observed in the upper part of the cloud. The liquid phase is characterized by LWC peaking at 0.1 g m^{-3}, droplet number concentrations around 75 cm^{-3}, and $D_{\mathrm{eff,w}}$ remaining below 20 μm. In particular, Norm-C clouds exhibit the lowest adiabatic ratios among all regimes (Fig. 9a), with values dropping below 0.5 at the base of the liquid layer and 0.2 near the cloud top. Such strongly sub-adiabatic profiles may indicate either enhanced consumption of liquid water through microphysical processes (*e.g.*, riming, evaporation, WBF process) or reduced efficiency in liquid water production. The IWC reaches 0.02 g m^{-3}, while ice crystals grow substantially from approximately 1000 μm near cloud top to over 2000 μm near cloud base. Ice number concentrations remain low (typically < 1 L^{-1}). Compared to WAA and Norm-W regimes, Norm-C shows marked differences in both the liquid and ice phases: ice crystals are much larger, pointing to a more efficient ice crystal growth. The increase in ice particle size, along with the gradual rise in IWC toward the lower part of the mixed-phase region, is consistent with sedimentation, with larger crystals dominating at lower levels.

https://doi.org/10.5194/egusphere-2026-3265
Preprint. Discussion started: 19 June 2026

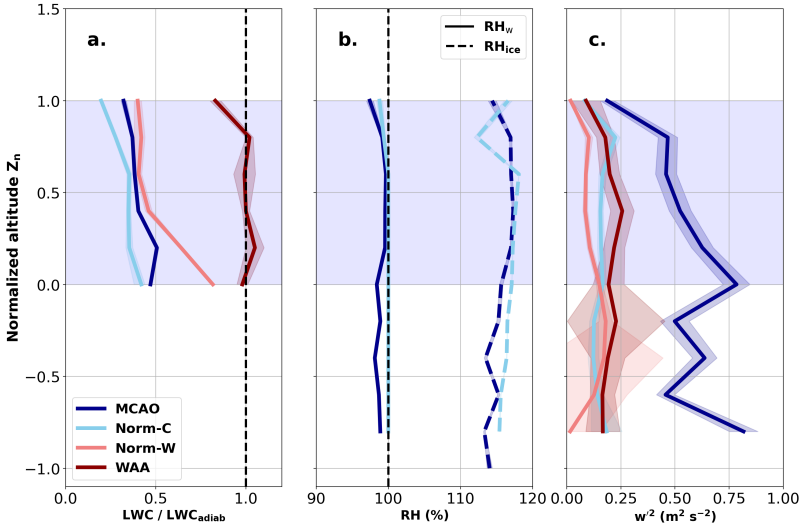

Figure 9. Normalized vertical profiles of **(a)** the ratio of *in situ* to adiabatic liquid water content ($\mathrm{LWC/LWC_{adiab}}$), **(b)** relative humidity from aircraft measurement (RH) and **(c)** variance of vertical velocity (w'^2) for different synoptic regimes: MCAO (dark blue), Normal-C (light blue), Normal-W (light coral), and WAA (dark red). Shaded areas indicate the 99 % confidence interval of the median. Note that RH measurements from ACLOUD were not used in panel **(b)**, as their absolute values are not considered reliable.

Under MCAO conditions, the cloud profiles reveal a well-organized mixed-phase system. In this regime, the environment is cold, with a median cloud-top temperature close to -16.5 °C, about 13 °C lower than under WAA conditions. Despite these low temperatures, $\mathrm{RH_w}$ remains consistently close to 98 % and $\mathrm{RH_{ice}}$ values indicate supersaturated conditions with respect to ice (> 110 %; Fig. 9b). This combination of cold and moist conditions provides a favorable setting for the coexistence of liquid water droplets and ice crystals. In the liquid phase, a relatively homogeneous layer extends throughout the cloud, similar to the Norm-C case. The LWC remains below 0.1 g $\mathrm{m^{-3}}$, while the extinction coefficient exhibits a pronounced maximum of about 16 $\mathrm{km^{-1}}$ near $Z_\mathrm{n} \approx 0.75$. Droplet concentrations range between 60 and 75 $\mathrm{cm^{-3}}$, with $D_{\mathrm{eff,w}}$ increasing toward the base of the liquid layer from 15–16 μm near the cloud top to ≈ 20 μm at $Z_\mathrm{n} = 0$. The ratio of $\mathrm{LWC/LWC_{adiab}}$ (Fig. 9a) decreases from 0.5 at the cloud base to about 0.3 near the top, reflecting sub-adiabatic conditions. MCAO clouds exhibit a more substantial ice component compared to Norm-C. The IWC increases markedly toward the surface, exceeding 0.06 g $\mathrm{m^{-3}}$ at Z_n = -1, while remaining below 0.02 g $\mathrm{m^{-3}}$ near the top of the liquid-containing layer. On average, IWC values are more than two to three times higher than under other meteorological conditions. The extinction coefficient follows a similar trend, from about 1 $\mathrm{km^{-1}}$ near cloud top to nearly 4 $\mathrm{km^{-1}}$ at lower levels. The ice crystal concentrations increase steeply from 0.8 $\mathrm{L^{-1}}$ near cloud top to 4 $\mathrm{L^{-1}}$ around $Z_\mathrm{n} = 0$, before stabilizing around 2 $\mathrm{L^{-1}}$ further down. $D_{\mathrm{eff,i}}$ decreases with altitude, increasing from about 1200 μm near cloud top to 1500 μm at the mixed-layer base, and exceeding 2500 μm at Z_n = -0.75. This vertical structure suggests the presence of a precipitating region in the lower cloud layers, characterized by large ice crystals, higher IWC, and sustained ice crystal concentrations. The simultaneous reduction in number and increase in size of crystals at lower levels is

https://doi.org/10.5194/egusphere-2026-3265
Preprint. Discussion started: 19 June 2026

typical of aggregation and riming processes (Maherndl et al., 2024; Schirmacher et al., 2024). This is consistent with the highly turbulent environments observed during MCAO events. This interpretation is further supported by turbulence measurements (TKE), with strong vertical velocity fluctuations w'^2 exceeding 0.4 m^2 s^{-2} throughout most of the cloud layer and reaching peak values up to 0.8 m^2 s^{-2}, indicative of a strongly turbulent regime.

Normalized vertical profiles of cloud microphysical properties (Fig. 8) reveal regime-dependent vertical structures that reflect not only the thermodynamic stability of the atmosphere but also the efficiency of underlying cloud microphysical processes. Each regime shows a characteristic vertical distribution of the liquid and ice phases. WAA clouds are characterized by abundant supercooled liquid water but inefficient glaciation, with weak coupling between the liquid and ice phases. In general, Norm-W clouds form in environments dominated by the liquid phase, with cloud temperatures sometimes exceeding 0 °C, which are therefore not favorable for the maintenance and development of the ice phase. Norm-C represents a transitional regime with more heterogeneous glaciation and moderate liquid–ice coupling. In contrast, MCAO clouds exhibit a strongly coupled mixed-phase system with efficient glaciation, substantial ice growth, and active precipitation processes.

3.2 Influence of temperature inversions

In this section, the analysis focuses on the role of temperature inversions and their influence on cloud microphysical properties for the two most distinctive regimes (MCAO and WAA). As previously highlighted in Figure 4b, WAA conditions are characterized by a frequent and pronounced occurrence of temperature inversions, which result in a strongly stratified boundary layer. In contrast, MCAO regimes, although generally associated with unstable atmospheric layers, can still exhibit locally strong temperature inversions within or near the top of the observed low-level clouds. To better capture this variability, cases are classified into weak and strong inversion regimes. This separation is based on the median inversion strength within each regime, with median values of 2.4 °C for MCAO conditions and 5.7 °C for WAA conditions.

Table 3 compares the macrophysical structure of the clouds observed during WAA and MCAO events as a function of the temperature inversion strength. Under the influence of WAAs, the median liquid cloud base remains close to 170 m, regardless of the inversion strength. However, for strong inversion cases, results show that the cloud top is lower (410 m), colder (-3.8 °C), and the cloud layer is thinner (250 m compared to 374 m for weak inversions).

Table 3. Macrophysical properties of clouds observed during WAA and MCAO events, categorized by temperature inversion. Values include the number of sampling legs (N_{leg}), in-cloud measurement time (t_{cld}), and the base (Z_{b}), top (Z_{t}), and thickness (H_{cld}) of the liquid-containing cloud layer, as well as the cloud-top temperature (T_{top}). Median values are shown with interquartile ranges in brackets.

MCAO	Inversion Regime	N_{leg}	t_{cld} (min)	Z_{b} (m)	Z_{t} (m)	H_{cld} (m)	T_{top} (°C)
WAA	WEAK (< 5.7 °C)	11	96	170 [100/350]	564 [440/820]	374 [270/435]	-2.2 [-4.1/-1.6]
	STRONG (> 5.7 °C)	19	228	170 [90/190]	410 [380/440]	250 [240/270]	-3.8 [-6.2/-2.4]
MCAO	WEAK (< 2.4 °C)	52	199	220 [130/390]	650 [520/850]	430 [240/520]	-16 [-17.5/-15.3]
	STRONG (> 2.4 °C)	84	422	320 [160/480]	650 [500/860]	390 [200/500]	-15.7 [-17.1/-12.8]

https://doi.org/10.5194/egusphere-2026-3265
Preprint. Discussion started: 19 June 2026

As expected, this suggests that stronger inversions tend to limit the vertical development and extent of low-level clouds. Conversely, weaker inversions may allow enhanced cloud-top entrainment and deeper vertical development, leading to larger cloud geometrical thicknesses. Figures 10 (a–d) show the associated vertical profiles of cloud microphysical properties. Under strong inversion conditions, the LWC values are high, reaching nearly 0.5 g m^{-3} in the upper part of the cloud, although they remain lower than the ones measured when a weaker temperature inversion occurs near cloud top, with a decrease of about 0.1 g m^{-3} (Fig. 10a; dotted lines). The cloud droplet effective diameter appears relatively similar in both regimes, with larger droplets found toward cloud top (around 22 μm; Fig. 10a) and smaller ones close to cloud base (13 μm).

The differences between the two inversion regimes are more pronounced for the ice phase (Fig. 10b–d). Strong inversion cases exhibit higher number and mass concentrations, as well as larger ice crystal sizes. Within the mixed-phase region ($0 < Z_n < 1$), ice number concentrations increase from 0.5 L^{-1} at the top to more than 1.5 L^{-1} near cloud base ($Z_n = 0$). This behavior is also observed for the ice crystal size ($D_{eff,i}$ which increases from 450 μm to 750 μm) and for IWC (increasing from 5 mg m^{-3} to more than 15 mg m^{-3} near cloud base).

The vertical structure of ice properties suggests that strong inversions may favor the maintenance of the ice phase, with nucleation occurring in the upper, colder part of the cloud, from which ice crystals grow throughout the lower layers and precipitate. During weaker temperature inversions, the ice phase is less present and well mixed within the cloud layers. N_i peaks at 0.3 L^{-1} in the coldest part of the profile ($Z_n = 0.75$) and does not exceed 1.5 L^{-1} in the precipitation layers where their effective dimension is larger than 700 μm. In contrast, the liquid phase properties appear to be less affected by the inversion strength during WAA events.

During MCAO conditions, the liquid phase is reduced compared to WAAs but is more strongly influenced by the strength of the cloud top temperature inversion (Fig. 10e). In the presence of strong inversions, the LWC is higher, reaching values up to 0.08 g m^{-3} in the upper cloud layers where the temperature inversion is the strongest ($Z_n \approx 0.75$). The size of the water droplet slightly decreases from 20 μm near the cloud top to 14 μm near cloud base. In contrast, a marked increase in droplet size is observed (up to 25 μm) in the lower part of the liquid layer when weaker temperature inversions occur. Table 3 also shows that the median thickness of the liquid water layer is reduced (around 390 m) under strong inversion conditions. The ice phase is more prevalent during MCAOs than during WAAs, although the strength of the temperature inversion only moderately influences the vertical distribution of the ice crystal properties. Indeed, under MCAO conditions, cloud top temperatures are already cold enough (close to -16 °C) to trigger the nucleation of ice crystals. Therefore, the strength of the temperature inversion does not appear to be a key factor in the production of ice crystals in the upper cloud layers. However, the lowest part of the mixed phase layer ($0 < Z_n < 0.5$) is characterized by a significant increase of the number concentration and IWC when the temperature inversion is weak (Fig. 10f-g). In this layer, N_i is typically larger than 3 L^{-1} compared to values lower than 1.5 or 2 L^{-1} when the temperature inversion is more pronounced. A maximum value of nearly 5 L^{-1} seems to occur at $Z_n = 0.2$, where the largest supercooled liquid water droplets are observed. In both cases, ice crystals with an effective dimension larger than 1500 μm are observed in the precipitation layers (Fig. 10h), although the crystals tend to be larger when the inversion is stronger.

https://doi.org/10.5194/egusphere-2026-3265
Preprint. Discussion started: 19 June 2026

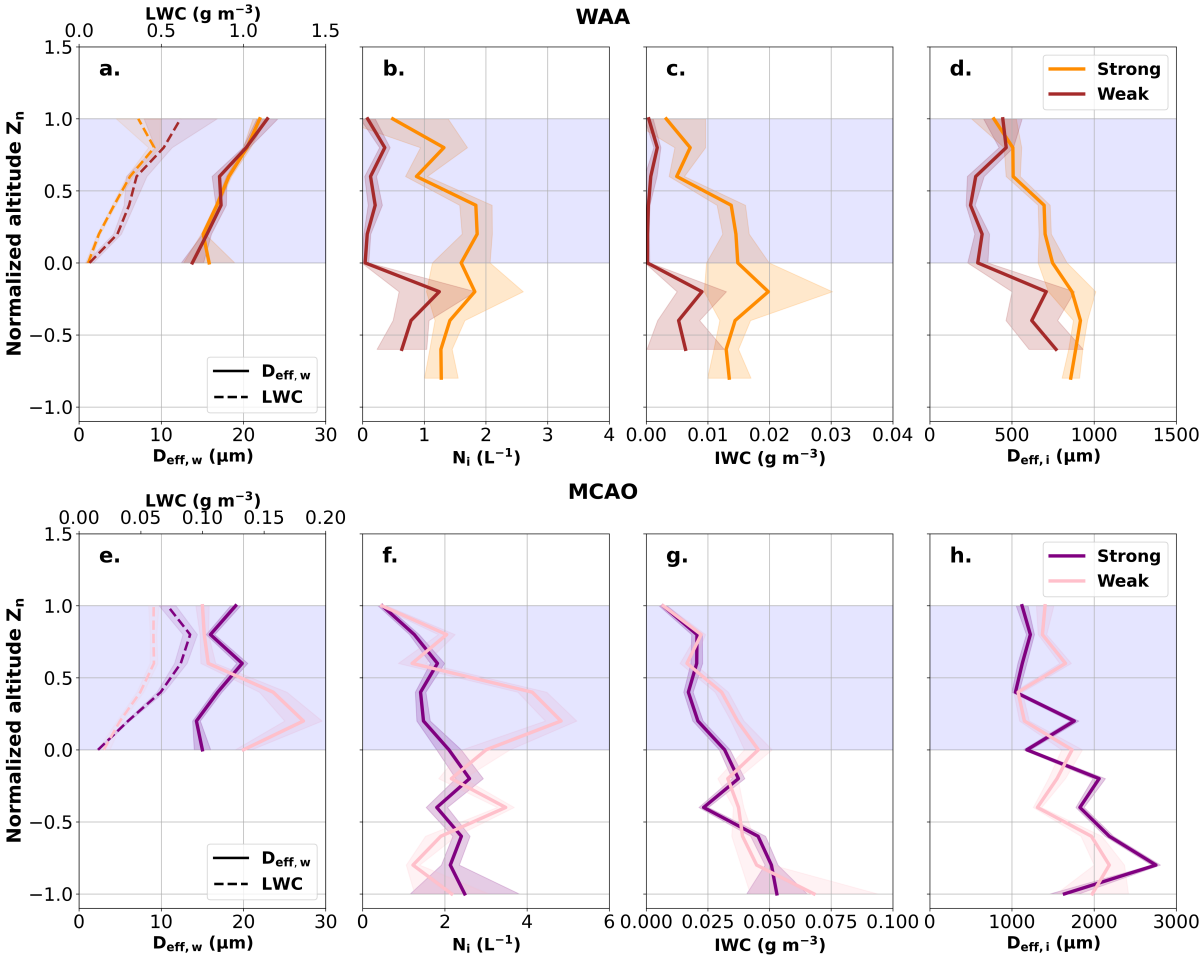

Figure 10. Normalized vertical profiles of droplet effective diameter ($D_{\mathrm{eff,w}}$) and liquid water content (LWC) (**a**, **e**), ice crystal concentration (N_{i}) larger than 50 μm (**b**, **f**), ice water content (IWC) (**c**, **g**), and ice effective diameter ($D_{\mathrm{eff,i}}$) larger than 50 μm (**d**, **h**) for WAA (top row) and MCAO (bottom row) under strong and weak inversion. Lines represent the median across profiles for each regime, and shaded envelopes indicate the 99 % confidence interval of the median.

3.3 Sea ice influence

In this subsection, we investigate the link between surface conditions and the microphysical and macrophysical properties of low-level mixed-phase clouds. The results focus on the differences observed between open ocean and sea ice under MCAO and WAA regimes. For clarity, WAA cases are first described over open ocean and then over sea ice, while the opposite order is adopted for MCAOs, consistent with the direction of air mass advection during the events.

During WAA conditions over the open ocean, the liquid phase predominates (Fig. 11a). The droplet number concentration N_{w} is greater than 125 cm^{-3} in nearly all the cloud layers, and the LWC reaches 0.75 g m^{-3} near the cloud top. This liquid

https://doi.org/10.5194/egusphere-2026-3265
Preprint. Discussion started: 19 June 2026

water-containing layer has a median base located at 300 m and a median top at 765 m. Figure 12 shows normalized profiles of sensible heat flux (H) for WAA and MCAO regimes over sea ice (SI) and open ocean (OO). This vertical structure is consistent with relatively weak surface forcing over OO, as shown by the sensible heat flux profile (Fig. 12a). Values remain close to 0 W m^{-2} near the liquid cloud base and increase only gradually upward, reaching about 10 W m^{-2}. This suggests a limited turbulent transport from the surface to the cloud layer. In contrast, ice-phase profiles indicate very low ice crystal number concentrations (< 0.1 L^{-1}) and IWC, associated with small non-precipitating ice crystals ($D_{\mathrm{eff,i}}$ < 300 μm). These results show that low-level clouds that evolve under WAA and over open water are almost entirely composed of liquid water droplets. The relatively warm cloud-top temperatures (median value around -2.1 °C) in these low-level clouds do not favor the development and maintenance of the ice phase.

Table 4. Macrophysical properties of clouds observed during WAA and MCAO events, categorized by surface type. Values include the number of sampling legs (N_{leg}), in-cloud measurement time (t_{cld}), and the base (Z_{b}), top (Z_{t}), and thickness (H_{cld}) of the liquid-containing cloud layer, as well as the cloud-top temperature (T_{top}). Median values are shown with interquartile ranges in brackets. Surface types correspond to open ocean (OO; SIC < 20 %) and sea ice (SI; SIC > 80 %).

MCAO regime	Type of surface	N_{leg}	t_{cld} (min)	Z_{b} (m)	Z_{t} (m)	H_{cld} (m)	T_{top} (°C)
WAA	OO (SIC < 20 %)	8	64	300 [50/380]	765 [630/870]	443 [420/580]	-2.1 [-4/-0.8]
	SI (SIC > 80 %)	22	217	170 [115/190]	410 [380/440]	250 [240/270]	-3.8 [-6.2/-2.4]
MCAO	OO (SIC < 20 %)	89	408	320 [220/430]	770 [650/860]	430 [330/520]	-15.3 [-16.7/-14.8]
	SI (SIC > 80 %)	36	94	230 [110/320]	540 [480/630]	290 [200/430]	-16.5 [-17.3/-14.7]

Over the sea ice, the properties of WAA clouds clearly shift towards higher concentrations of ice crystals (N_{i} > 50 μm), at the expense of the liquid water phase. The liquid water-containing layer becomes geometrically thinner (≈ 250 m), with a lower and colder cloud top, which may favor heterogeneous nucleation (410 m and T_{top} ≈ -3.8 °C). Both N_{w} and LWC remain high but decrease significantly (LWC < 0.4 g m^{-3} and N_{w} < 110 cm^{-3}, respectively).

These clouds are associated with even weaker surface-atmosphere exchanges, with sensible heat flux values remaining below 4 W m^{-2} between the surface and the liquid cloud base and increasing only slightly within the liquid layer, up to about 6 W m^{-2}. These values are consistent with those reported by Chechin et al. (2023), highlighting the limited turbulent heat exchange over sea-ice-covered surfaces. This weak vertical increase suggests a limited supply of heat and moisture from the surface layer. This weak vertical increase suggests a limited supply of heat and moisture from the surface layer. The contribution of the ice phase increases from the cloud top to the surface: concentrations and size remain relatively low near the cloud top (Z_{n} = 1, N_{i} ≈ 0.5 L^{-1} and $D_{\mathrm{eff,i}}$ ≈ 500 μm), but increase below the mixed-phase layer (Z_{n} < 0), where IWC reaches 0.02 g m^{-3} and ice crystals become significantly larger ($D_{\mathrm{eff,i}}$ > 800 μm).

During MCAO events, clouds over sea ice evolve in a cold environment (T_{top} ≈ -16.5 °C), with a mixed-phase layer typically bounded by a median top located at 540 m and a base at 230 m. This layer is characterized by an LWC peak near the cloud top (LWC ≈ 0.1 g m^{-3} at Z_{n} ≈ 0.75) and with droplet concentrations around 80 cm^{-3} (Fig. 11e). Relatively low concentrations of small ice crystals (< 1 L^{-1}) of sizes up to 700 μm are detected in the upper part of the cloud layer. A peak in ice crystal

https://doi.org/10.5194/egusphere-2026-3265
Preprint. Discussion started: 19 June 2026

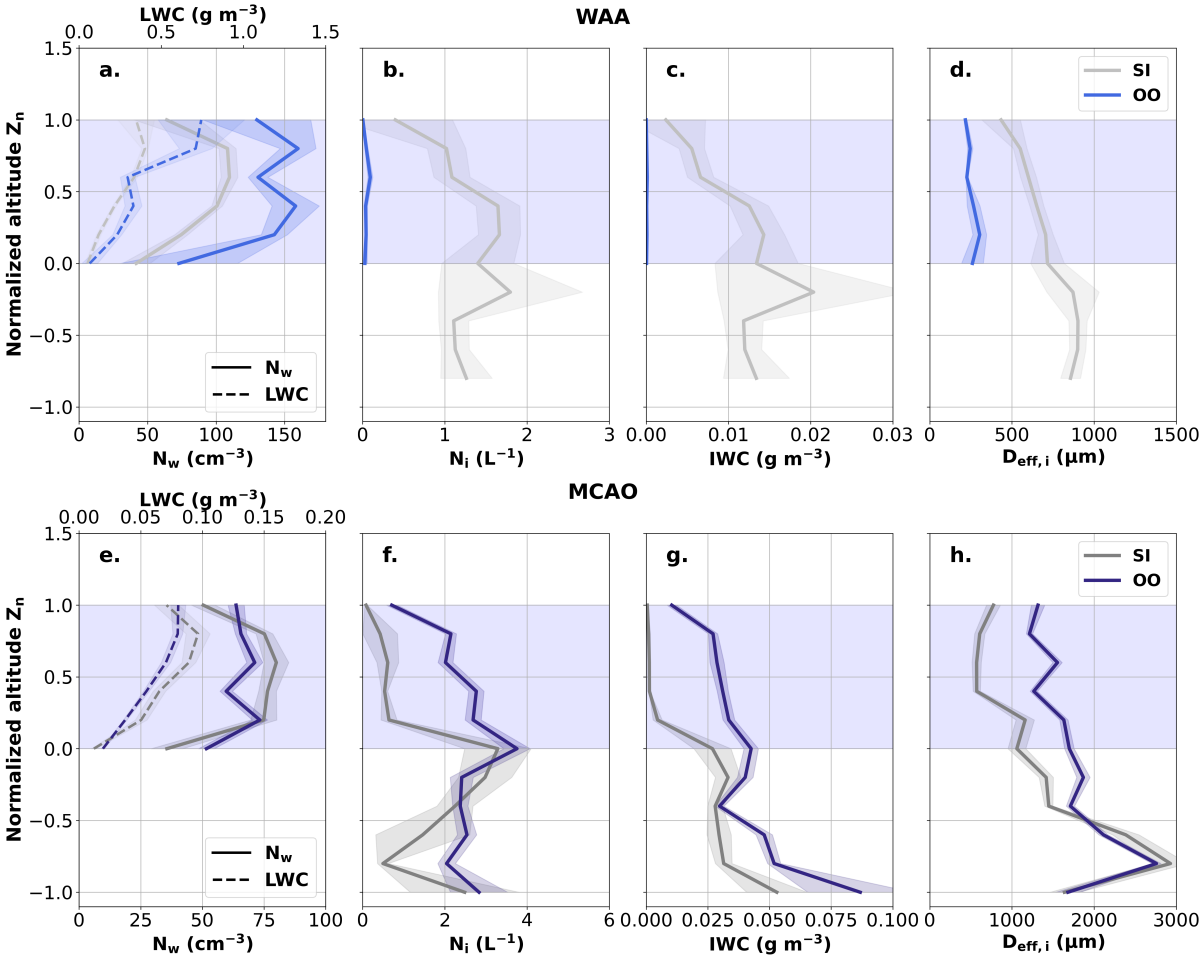

Figure 11. Normalized vertical profiles of droplet concentration (N_w) and liquid water content (LWC) (**a**, **e**), ice crystal concentration (N_i) (**b**, **f**), ice water content (IWC) (**c**, **g**), and ice effective diameter ($D_{eff,i}$) larger than 50 μm (**d**, **h**) for WAA (top row) and MCAO (bottom row) over sea ice (SI) and open ocean (OO). Lines represent the median across profiles for each regime, and shaded envelopes indicate the 99 % confidence interval of the median.

concentration (2.5 L^{-1}) is observed near the base of the liquid-containing layer ($Z_n = 0$). Below this level, N_i decreases sharply toward the surface while IWC increases ($\approx$ 0.05 g m^{-3}, Fig. 11g), pointing to efficient growth of precipitating ice particles. Indeed, Figure 11h shows that ice crystals grow to size up to 2 mm in the lower part of the profile (Z_n < -0.5), a characteristic value of snow precipitation. Over sea ice, sensible heat fluxes remain relatively weak throughout the vertical profile, generally below 5 W m^{-2}, with only a few localized peaks.

As the air mass is transported over the open ocean, the liquid layer becomes geometrically thicker (430 m), with a higher cloud top (770 m) and slightly warmer temperatures (-15.3 °C) compared to clouds over sea ice. These macrophysical changes are coupled with a slight decrease in LWC and N_w throughout the cloud and an enhanced ice phase. The concentrations of

https://doi.org/10.5194/egusphere-2026-3265
Preprint. Discussion started: 19 June 2026

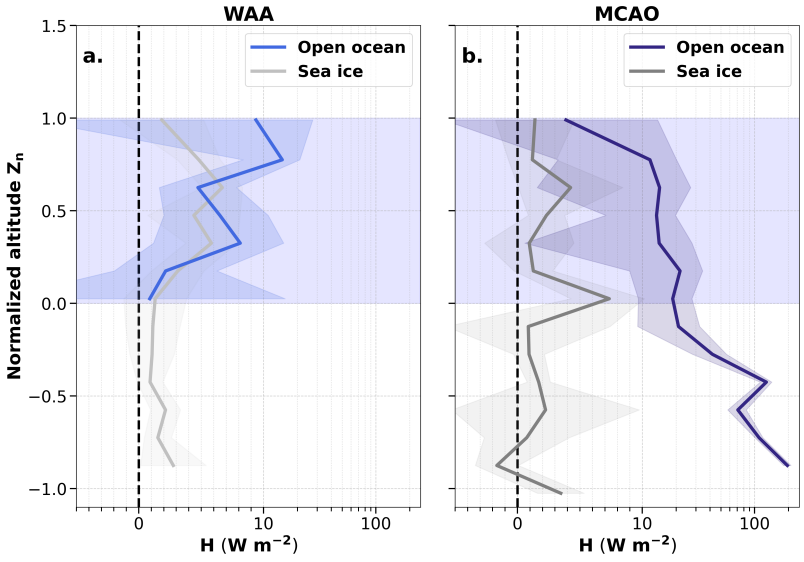

Figure 12. Normalized vertical profiles of sensible heat flux (H) for MCAO and WAA regimes over sea ice (SI; SIC > 80 %) and open ocean (OO; SIC < 20 %). Lines represent the median across profiles for each regime, and shaded envelopes indicate the 99 % confidence interval of the median.

ice crystals increase from cloud top to cloud base, reaching a maximum of 4 L^{-1} near $Z_n = 0$. The effective diameter already exceeds 1100 μm near the top of the liquid layer, indicating efficient growth processes. In the lower part of the cloud, high concentrations (> 2 L^{-1}) combined with large crystal sizes (larger than 2 mm) lead to significant ice water contents (IWC > 0.08 g m^{-3}), consistent with sustained precipitation. The sensible surface heat fluxes are substantially higher during MCAO conditions than under WAA conditions, with values approaching 200 W m^{-2} near the surface. These fluxes decrease with altitude and reach much lower values in the upper part of the cloud, around 5 W m^{-2}.

To further investigate the influence of turbulent motions on the vertical distribution of microphysical properties, turbulent kinetic energy (TKE) and vertical wind velocity (w) are determined for the different types of surface and meteorological conditions (WAAs and MCAOs) in Figure 13. MCAO conditions (Fig. 13c-d) are characterized by a more turbulent environment compared to WAAs (Fig. 13a-b). Over the open ocean, the median TKE reaches 0.50 m^2 s^{-2} during MCAOs, compared to 0.35 m^2 s^{-2} under WAA conditions. In addition, the MCAOs distribution is skewed towards higher values, with the third quartile reaching 1.01 m^2 s^{-2}, highlighting the presence of strongly turbulent conditions. In contrast, TKE distributions during WAAs are less dispersed and are centered around their median values, particularly over sea ice (0.26 m^2 s^{-2}). This feature is a signature of weaker and more homogeneous turbulence. During WAAs, the median vertical velocities are low, regardless of the surface type. The updraft speeds are around 0.35 m s^{-1} and -0.22 m s^{-1} to -0.24 m s^{-1} for downdrafts. In contrast, under MCAO conditions the distribution of vertical motions is broader and varies more with the surface type. Downdrafts are more intense over the open ocean with median values of -0.32 m s^{-1} and a larger inter-quartile range, compared to a median value of -0.22 m s^{-1} over sea ice. Overall, these results confirm that MCAO conditions are associated with a stronger turbulent envi-

https://doi.org/10.5194/egusphere-2026-3265
Preprint. Discussion started: 19 June 2026

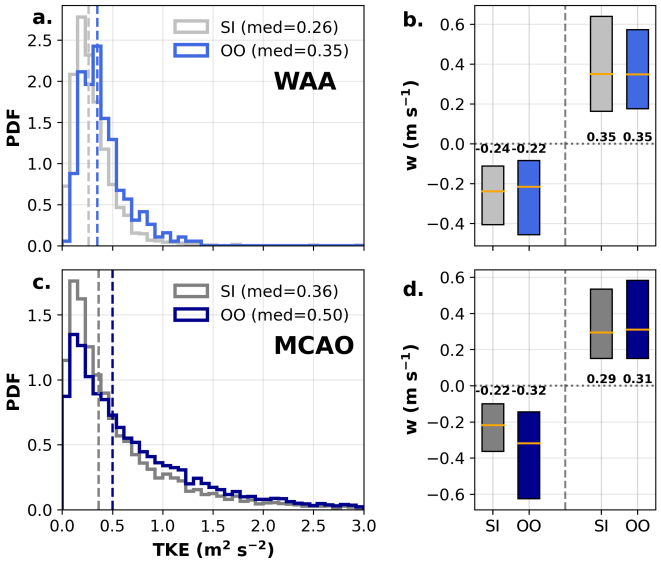

Figure 13. Probability density functions (PDFs) of turbulent kinetic energy (TKE, left panels) and boxplots of vertical velocity (w, right panels) for WAA (**a**–**b**) and MCAO (**c**–**d**) regimes over sea ice (SI) and open ocean (OO). In the right panels, positive and negative values of w correspond to updrafts ($w > 0$ m s^{-1}) and downdrafts ($w < 0$ m s^{-1}), respectively. Values indicated on the boxplots correspond to median vertical velocities.

ronment, further intensified over open ocean. These stronger updrafts and downdrafts promote more efficient vertical mixing and redistribution of water vapor, cloud droplets, and ice crystals within the cloud layer. This enhanced mixing can favor both ice crystal growth and precipitation and may also influence the development of different crystal morphologies.

4 Ice crystal habits

In this section, an analysis of the morphological characteristics of ice particles is carried out to provide insight into the microphysical processes occurring in MPCs. Specifically, the vertical distributions of ice crystal habits observed during the four campaigns are investigated for different contrasting large-scale regimes (*e.g.*, MCAOs vs. WAAs) and surface types (open ocean vs. sea ice). The analysis is based on instantaneous crystal images collected during aircraft transects, which provide a view of the sampled particles.

The vertical and temperature-dependent distributions of the morphological classes of ice crystals, derived from a CNN classifier (Jaffeux et al., 2022), are presented in Figure 14. Panels show the morphological fractions as a function of normalized altitude (Fig. 14a-b) and temperature (Fig. 14c-d), for small (300-1280 μm) and large particles (2000-6400 μm), separately. This figure highlights the large diversity of ice crystal habits observed within the different cloud layers. The number of classified images in each temperature and normalized altitude bin is provided in Figure S4 in the Supplement. Color shades are used to

https://doi.org/10.5194/egusphere-2026-3265
Preprint. Discussion started: 19 June 2026

reflect morphologies that share similar formation or growth processes, such as vapor deposition (green shades), riming (brown shades), or aggregation (blue shades) to facilitate interpretation in terms of underlying microphysical mechanisms.

4.1 Overview for all campaigns

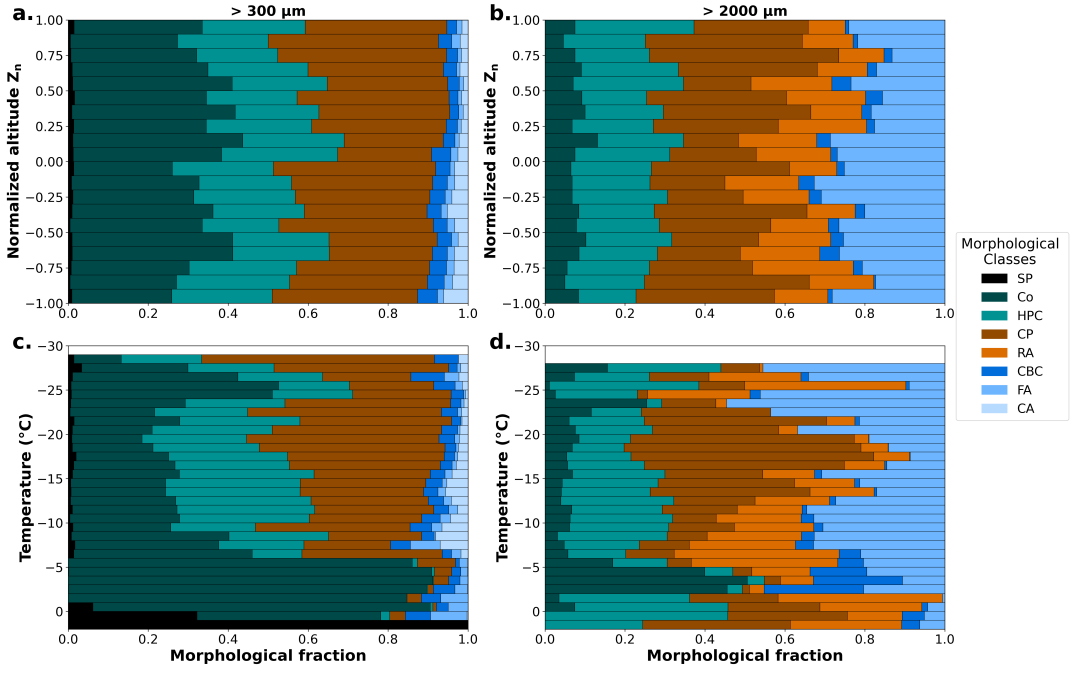

Figure 14. Morphological number fraction distribution of hydrometeors for small crystals (> 300 μm) and precipitating crystals (> 2000 μm). Subplots (**a**) and (**b**) illustrate the morphological fraction as a function of normalized altitude (Z_n). Panels **(c)** and **(d)** depict the morphological fraction as a function of temperature (°C). Morphological classes are : Spherical Particle (SP), Column (Co), Hexagonal Planar Crystal (HPC), Compact Particle (CP), Rimed Aggregates (RA), Combination of Bullets or Columns (CBC), Fragile Aggregates (FA), and Complex Assemblages (CA).

Pristine Ice Crystals

Columnar ice crystals (Co) exhibit two main temperature-dependent peaks: one located between 0 °C and –5 °C, accounting for 80–90 % of the population of small ice crystals, and another near –25 °C, representing approximately 50 % of the ice particles at this temperature (Fig. 14c). These peaks appear in both small particles and precipitating crystals (Fig. 14d), although their relative abundance is lower for larger particles (< 50 %). The proportion of columns remains fairly constant with altitude, representing 30 % of small ice particles. This proportion drops below 10 % for precipitating particles. Hexagonal Planar Crystals (HPC) occur mainly between –8 °C and –15 °C, reaching a fraction of 20 % in both crystal size ranges. Large HPCs, probably falling from colder cloud layers, are also occasionally found near 0 °C. The fraction of HPC remains relatively constant throughout the cloud column (15–20 %), with a slight decrease observed near the surface (Z_n = -0.75 to -1).

https://doi.org/10.5194/egusphere-2026-3265
Preprint. Discussion started: 19 June 2026

These habit distributions are in agreement with classical habit diagrams (Nakaya, 1954; Bailey and Hallett, 2004) and Arctic *in situ* observations that show the prevalence of columnar and planar forms in similar temperature ranges (Järvinen et al., 2023).

Aggregated Particles

Ice crystal aggregates, including Combination of Bullets or Columns (CBC), Fragile Aggregates (FA), and Complex Assemblages (CA), form a substantial part of the ice population, particularly in the lower cloud and precipitation layers. The number fraction of small aggregates reaches a maximum near 0 °C (Fig. 14c). This temperature range is associated with efficient particle sticking (Phillips et al., 2015), which may contribute to the formation of CBC particles. A second maximum is observed at –10 °C, where dendritic plates interlock efficiently (Chellini and Kneifel, 2024). These two modes account for 15–20 % of the total population of small ice crystals at these temperatures. The most common shape observed are complex assemblage (CA) crystals. Figure 14a shows that the aggregate fraction increases below the liquid-containing layer ($Z_{\mathrm{n}} < 0$). This feature is consistent with the enhanced aggregation observed in the ice precipitation layer. Large aggregates (> 2000 μm) contribute up to 45 % of the population of large ice crystals. This is particularly true at temperatures close to -5 °C, where CBC are usually found. More generally, results show that aggregates account for more than 15 % of ice crystals throughout the column and for 35–40 % near cloud base. These findings confirm that aggregation is one of the key mechanisms responsible for the growth and sedimentation of ice crystals in low-level Arctic mixed-phase clouds.

Rimed Particles

Compact particles (CP) and rimed aggregates (RA) are observed throughout the cloud. These morphologies are typically associated with ice crystals that have undergone moderate to heavy riming or that have grown rapidly under environmental conditions that limit the development of pristine ice crystals. CP dominates a large part of the cloud column, with slightly higher occurrence found in the upper cloud layers where these crystals represent up to 30–40 % of the number of small ice particles. In the upper half of the mixed-phase layer, the presence of relatively high LWC promotes the droplet-ice interactions, which can lead to efficient riming of ice crystals. The combined contribution of large compact precipitating particles and rimed aggregates exceeds 50 % of the total morphological fraction. This result highlights the prevalence of riming among the precipitating population. Figure 14d shows a sharp peak in the occurrence of CP that reaches more than 60 % near –20 °C. Rimed aggregates are characterized by two distinct peaks: one near –7.5 °C and another around –25 °C. These peaks likely correspond to regions where aggregation is followed by intense riming, allowing ice crystals to grow rapidly in size and mass. The presence of rimed aggregates (RA) is a signature of ice particles formed through a combination of growth mechanisms, including aggregation and subsequent riming.

In addition, spherical particles (black) are identified, representing drizzle particles ($\approx$ 300 μm). Their presence is strongest at temperatures above 0 °C, but they also occur sporadically at colder temperatures (*e.g.*, near –6 °C or –27 °C). These occurrences are rare and correspond to a very small percentage corresponding to the formation and persistence of drizzle drops within mixed-phase layers.

In general, classification reveals clear dependencies of crystal habit with temperature and altitude in mixed-phase clouds. Pris-

https://doi.org/10.5194/egusphere-2026-3265
Preprint. Discussion started: 19 June 2026

tine crystals (columns and plates) dominate within characteristic growth temperature ranges, with columnar crystals showing distinct peaks around -4 °C and -25 °C. Aggregation and riming processes prevail in lower layers and in the precipitation zone. The strong presence of rimed and aggregated habits emphasizes efficient droplet–ice crystal interactions that control particle growth and precipitation formation within low-level Arctic clouds.

4.2 Comparison of ice crystal habits between MCAO and WAA regimes

Here, the analysis focuses on the variability of ice crystal morphological properties for two distinct synoptic regimes: MCAOs and WAAs. As shown in Table 2, the thermodynamic structure of these two regimes, particularly the cloud-top temperature, differs significantly and is expected to impact the distribution of crystal habits and their associated growth mechanisms. Figure 15 shows the vertical distributions of the habit mass fractions for each regime, while the attached subplots present moving averages of the main growth processes. The number of classified images in each temperature and normalized altitude bin is provided in Figure S5 in the Supplement.

During MCAO events (Fig. 15a), rimed particles dominate the population of small ice crystals, representing approximately 50 % of the total mass fraction of ice crystals. The fraction of compact particles (CP) increases in the upper part of the cloud (Z_{n} between 0 and 1). There, riming is favored by the presence of supercooled liquid droplets in a turbulent environment. Aggregated particles account for less than 10 % of the mass fraction near cloud-top but exceed 15 % closer to the surface, indicating that aggregation becomes more efficient along the cloud depth. In contrast, pristine crystals are more abundant in the upper cloud layers (15 % Co and 30 % HPC) compared to roughly 40 % near the cloud base. The occurrence of HPC is typically associated with colder temperatures (around –15 °C), suggesting that these pristine habits are gradually transformed through aggregation (CA) or riming as they fall through the mixed-phase layer. For large particles, the proportion of columnar forms (Co) is very small (< 5 %) compared to hexagonal plate crystals which account for 15 % of the mass of precipitating ice crystals (Fig. 15c). Large pristine and aggregated ice crystals occur in similar proportions (≈ 20 %), while rimed particles account for 50% to 60 % of the total mass fraction of precipitating hydrometeors.

Mixed-phased clouds influenced by WAA conditions are dominated by small ice crystals with a columnar shape. These columns represent more than 80% of the total mass of small ice crystals (Fig. 15b). The mass proportion of these ice crystals decreases slightly from 95 % near the cloud top to approximately 80 % close to the underlying surface. As shown in Figure 4a and Table 2, WAA clouds are relatively warm with a cloud-top temperature of –3.3 °C. This temperature range coincides with that at which columnar crystals are most frequently observed according to Bailey and Hallett (2009). Our results also show that the observed gradual decrease in the column fraction with decreasing altitude is accompanied by an increase in the proportion of aggregated particles, particularly clusters of CBC, which reach up to 15 % near the cloud base. The fraction of strongly rimed particles (*e.g.*, CP) remains very small (< 10 %) despite the high liquid water content in the mixed-phase layer. Using high-resolution PHIPS (Particle Habit Imaging and Polar Scattering) observations, Järvinen et al. (2023) reported slight riming on columnar particles within WAA clouds, suggesting that such subtle riming features cannot be fully resolved by the 2D-S resolution (10 μm pixel size). This limited riming is consistent with relatively weak turbulent motions encountered in WAA conditions that limit the efficiency of droplet–ice interactions.

https://doi.org/10.5194/egusphere-2026-3265
Preprint. Discussion started: 19 June 2026

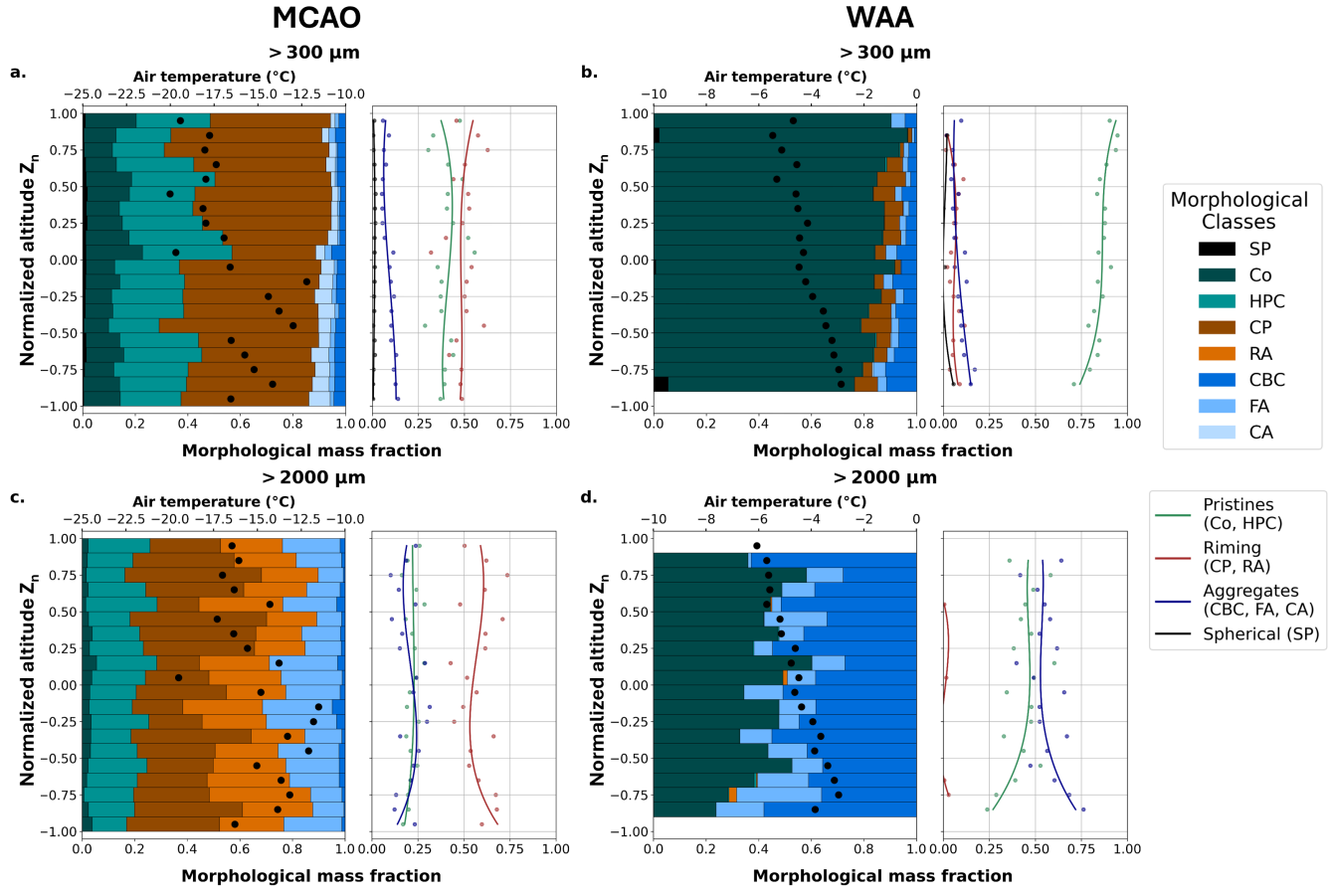

Figure 15. Vertical distribution of morphological mass fractions for small (**a**–**b**; > 300 μm) and precipitating (**c**–**d**; > 2000 μm) ice particles during (**a**–**c**) MCAO and (**b**–**d**) WAA regimes. Colors indicate different morphological classes: shades of green represent pristine crystals, brown tones correspond to rimed particles, blue tones denote aggregated forms, and black indicates spherical particles associated with drizzle water droplets. The line plots on the right of each panel show the vertically resolved mean morphological mass fractions for these process-based groups. Black dots represent the mean temperature profile derived from the aircraft measurements. Morphological classes are: Spherical Particle (SP), Column (Co), Hexagonal Planar Crystal (HPC), Compact Particle (CP), Rimed Aggregates (RA), Combination of Bullets or Columns (CBC), Fragile Aggregates (FA), and Complex Assemblages (CA).

Columnar habits still represent a large fraction of precipitating large crystals (2–6.4 mm), although their proportion drops from 45 % near cloud top to 30 % closer to the surface (Fig. 15d). This decrease is coupled with an increase in aggregates, with a strong presence of CBC (≈ 40 %) and fragile aggregates (≈ 15 %). Large particles do not show significant riming signatures. The prevalence of columnar and aggregated habits under WAA reflects a relatively quiescent and weakly turbulent environment, where crystal growth by vapor deposition and aggregation dominate over riming processes.

MCAO and WAA clouds exhibit distinct profiles of ice crystal morphological properties. MCAO clouds are dominated by compact and rimed particles, indicating intense growth by riming. In contrast, WAA clouds largely consist of pristine

https://doi.org/10.5194/egusphere-2026-3265
Preprint. Discussion started: 19 June 2026

or aggregated columnar forms. Precipitating aggregates are more prevalent in WAA clouds. These differences emphasize that rimed habits are a distinctive feature of MCAO clouds, while columnar and aggregated shapes are characteristics of clouds evolving under WAA conditions. Despite higher liquid water contents under WAA conditions, the fraction of rimed particles remains significantly lower, suggesting that riming efficiency is not solely controlled by liquid availability but may be influenced by droplet size and turbulence.

4.3 Surface influence during cold air outbreak

In this section, we investigate the morphological properties of cloud particles over different types of surface during MCAO events. A similar surface-based comparison under WAA conditions is not possible because ice crystals are very sparse, or nearly absent, over open ocean in that regime. Figure 16 presents the vertical distribution of morphological mass fractions segregated by surface type: open ocean (OO; SIC < 20%) and ice-covered regions (MIZ + SI; SIC > 20%). The number of classified images in each temperature and normalized altitude bin is provided in Figure S6 in the Supplement. The attached subplots further show moving averages of the main growth processes. Marginal ice zones and sea ice were combined into a single ice-covered surface because the respective vertical profiles of cloud particles exhibit similar morphological characteristics. From a thermodynamic perspective, the comparison between these surface types is not driven by large differences in cloud-top temperature, as median values remain similar (-16.5 °C in region covered by sea ice and -15.3 °C over the open ocean, Tab. 4).

Figure 16a shows that in the upper part of OO clouds (near $Z_n = 1$), the heavily rimed particles (CP) represent nearly 65 % of the small ice crystal population. This fraction gradually decreases towards the surface to approximately 50 %. This is consistent with observations of larger mass fraction of rimed particles within the liquid water-containing layer, where riming processes are potentially favored. For large particles (> 2000 μm), the contribution of pristine crystal habits decreases markedly, with columnar crystals becoming nearly absent and plate particles representing less than 20 % of the mass fraction. Rimed particles remain strongly represented in this size range, accounting on average for about 60 % of the mass fraction. Figure 16c also shows that aggregates and pristine crystals contribute almost equally ($\approx$ 20 % each) to precipitation-sized particles.

In contrast, clouds over MIZ and SI are characterized by a greater occurrence of dendritic and hexagonal plate crystals, accounting for 30–40 % of the mass of small ice particles (Fig. 16b). Together with the contribution of columnar crystals ($\approx$ 20 %), pristine crystal habits represent nearly 60 % of the mass fraction near the cloud top ($Z_n = 1$). A higher proportion of small aggregated particles is observed in the lower part of the profile ($\approx$ 15 %). As observed during OO conditions, rimed particles (CP) are more frequent within the liquid-containing layer, reaching nearly 40 %, but their overall mass fraction remains about 30 % lower over ice-covered surfaces. Among large particles, pristine crystal habits (columns and plates/dendrites) remain more prevalent over sea ice, contributing up to 30 % of the mass fraction. Ice crystal growth by aggregation is also evident, as the proportion of large aggregates exceeding 2 mm reaches 40 % near cloud top and 30 % near cloud base ($Z_n = 0$; Fig. 16d). The fraction of aggregated particles (CBC and FA) varies consistently with the presence of pristine crystals, particularly with columnar particles and their combinations. In contrast to OO conditions, the mass fraction of rimed particles is lower near the cloud top over ice-covered surfaces ($\approx$ 30 % compared to $\approx$ 60 % over OO).

https://doi.org/10.5194/egusphere-2026-3265
Preprint. Discussion started: 19 June 2026

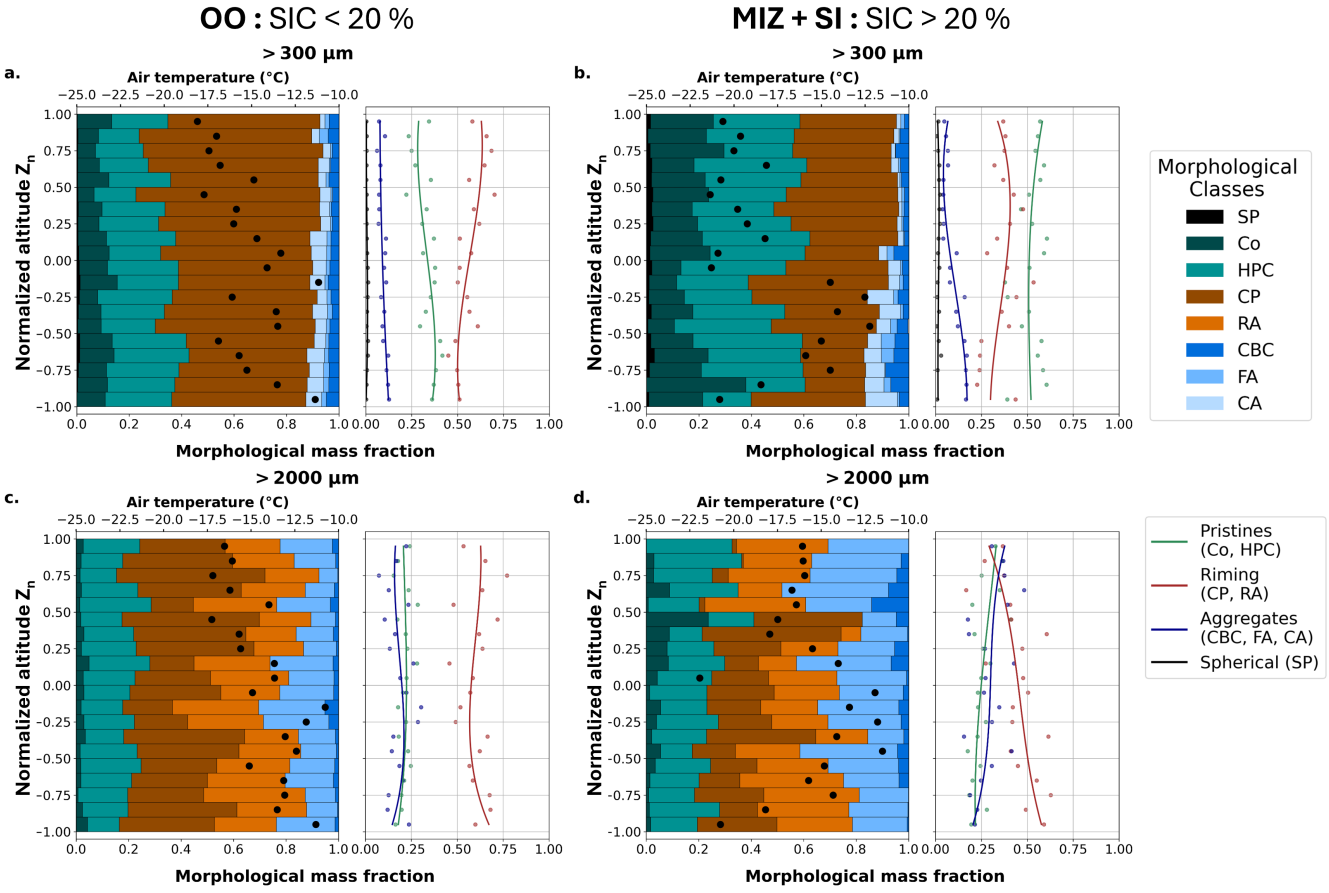

Figure 16. Vertical distribution of morphological mass fractions for small (**a**–**b**; > 300 μm) and precipitating (**c**–**d**; > 2000 μm) ice particles during MCAO, separated by surface type: (**a**–**c**) over open ocean (OO) and (**b**–**d**) over marginal ice zone and sea ice (MIZ and SI). Colors indicate different morphological classes: shades of green represent pristine crystals, brown tones correspond to rimed particles, blue tones denote aggregated forms, and black indicates spherical particles associated with supercooled water droplets. The line plots on the right of each panel show the vertically resolved mean morphological mass fractions for these process-based groups. Black dots represent the mean temperature profile derived from the aircraft measurements. Morphological classes are: Spherical Particle (SP), Column (Co), Hexagonal Planar Crystal (HPC), Compact Particle (CP), Rimed Aggregates (RA), Combination of Bullets or Columns (CBC), Fragile Aggregates (FA), and Complex Assemblages (CA).

5 Discussion

Compared to previous studies relying on shorter field campaigns or exclusively on remote sensing observations (Shupe et al., 2005, 2011; Young et al., 2017), this combined dataset offers an extended and process-oriented view of cloud microphysics across contrasted synoptic regimes. Our results confirmed that the vertical distribution of LWC is characterized by a decrease in $\mathrm{LWC}/\mathrm{LWC}_{\mathrm{adiab}}$ towards the cloud top (Fig. 9). This finding is consistent with the previous work by Jackson et al. (2012), who

https://doi.org/10.5194/egusphere-2026-3265
Preprint. Discussion started: 19 June 2026

reported a similar reduction in the adiabatic ratio near the top of Arctic mixed-phase clouds. This behavior likely reflects the combined effects of entrainment and microphysical processes. The moisture supplied from below is progressively consumed within the lower part of the cloud layer. During MCAO conditions, a substantial increase in IWC and ice crystal size is observed from the cloud top to the surface (Fig. 8). This behavior is consistent with that reported in Jackson et al. (2012) for cloud temperatures ranging from –10 to –15 °C (corresponding to the temperature range observed during MCAO events). This vertical structure suggests that ice growth and precipitation formation are efficient processes in the lower part of the cloud.

Mioche et al. (2017) also analyzed the vertical profiles of cloud microphysical properties influenced by northerly cold air masses. Although their study was limited to low-level MPCs over the open ocean, they reported a similar distribution of liquid-phase properties. Their results show greater differences in the ice precipitation layers (effective size and extinction coefficient), mainly due to the size limitation of the imaging probe used at the time. Our study benefits from improved measurement techniques, offering more robust and quantitative estimates of the effective size of ice crystals. These new measurements allow for a more accurate characterization of the vertical variability of ice particle size distribution. Consistent with our results, observations from the AFLUX and MOSAiC-ACA campaigns, reported by Moser et al. (2023b) showed that particles smaller than 50 μm are more abundant above sea ice, whereas larger crystals are preferentially found over the open ocean (Fig. 11). These findings support the hypothesis that surface conditions (and related surface fluxes) modulate the shape of particle size distributions and the associated microphysical processes, as previously suggested by Young et al. (2017) during the Aerosol-Cloud Coupling and Climate Interactions in the Arctic (ACCACIA) campaign.

Our study did not directly investigate the influence of aerosol particle loading associated with large-scale air mass advection on the cloud phase partitioning. However, aerosol properties derived from UHSAS measurements show that median aerosol number concentrations are lower during MCAO conditions (88 [78–135] cm^{-3}, where brackets indicate the interquartile range) compared to WAA cases (134 [131–160] cm^{-3}). This suggests that WAAs transport a greater quantity of aerosols, which may contribute to the observed increase in cloud droplet concentrations and, to a lesser extent, to the decrease in their effective diameter. The influence of aerosol particle number concentrations on cloud thermodynamic phase partitioning has also been highlighted by Arteaga et al. (2024) during flight 19 of the ACLOUD campaign. These observations are consistent with the well-established sensitivity of cloud droplet number concentration to aerosol availability (Dada et al., 2022; Lackner et al., 2023). In contrast, MCAO conditions are associated with lower aerosol concentrations as a result of air masses primarily originating from the relatively pristine Arctic Ocean (Lloyd et al., 2018; Sanchez et al., 2022). This reduced number of aerosols may limit the concentration of cloud droplets and influence the overall cloud microphysical structure (Morrison et al., 2012). More recently, Moser et al. (2025) showed that the underlying surface appears to influence both the size and concentration of available aerosol particles in Arctic low-level cloud environments.

Our observations of the variability in ice crystal habits (Fig. 14) are consistent with the results derived from the classical temperature-dependent habit diagrams (Nakaya, 1954; Bailey and Hallett, 2009). However, our measurements do not enable us to establish the life cycle history of the ice crystals. Consequently, the shape of the observed ice crystals may reflect not only their dependence on the local temperature and humidity at the sampling location but also the cumulative effects of the

https://doi.org/10.5194/egusphere-2026-3265
Preprint. Discussion started: 19 June 2026

variability of the thermodynamic conditions they experienced during their ascent and descent through the cloud layers. This could introduce biases when interpreting the relationship between ice crystal habit and cloud temperature.

Our results show a high occurrence of rimed and irregular particles, particularly when clouds evolve under MCAO conditions (Fig. 15). These shapes highlight strong droplet-ice interactions linked to the variability of turbulence and supersaturation in Arctic boundary-layer clouds. The strong contrast observed between the MCAO and WAA regimes is consistent with previous studies that have emphasized the importance of large-scale forcing in controlling the structure of Arctic clouds (Lackner et al., 2023). MCAO conditions favor turbulent boundary layers and enhanced surface heat and moisture fluxes, promoting ice production, riming, and precipitation (Schirmacher et al., 2023; Slättberg et al., 2025). Moreover, our results show that these dynamical regimes also produce distinct signatures in ice crystal habits and size distributions (Young et al., 2017; Moser et al., 2023a, 2025). In contrast, WAA cases are associated with strong low-level temperature inversions that reduce vertical mixing, resulting in thinner, predominantly liquid layers (Chechin and Lüpkes, 2017; Järvinen et al., 2023). Based on observations from ACLOUD and SOCRATES campaigns (Southern Ocean Clouds, Radiation, Aerosol Transport Experimental Study), Waitz et al. (2022) reports riming fractions of approximately 40 %, with a marked decrease in the detected icing fraction for smaller particles, particularly those smaller than approximately 300 μm. This size dependence suggests that riming may become increasingly difficult to identify in OAP images as particle size decreases, since small-scale surface features and small accreted droplets are less well resolved.

The results highlight the important role of turbulence in shaping both the microphysical properties and the habit of ice crystals in Arctic mixed-phase clouds (Brooks et al., 2017; Chechin et al., 2023). Turbulent motions enhance vertical mixing, favoring the continuous resupply of moisture and liquid water, while also promoting supersaturation fluctuations that influence ice growth processes. These conditions can help maintain the coexistence of multiple growth regimes and contribute to the formation of irregular and rimed particles, particularly in dynamically active environments such as MCAO cases (Chellini and Kneifel, 2024; Maherndl et al., 2024). In addition, turbulence may modulate particle collision rates and aggregation processes, further affecting the ice crystal size distribution and habits.

Overall, this study provides a statistical characterization of the mean microphysical properties of Arctic mixed-phase clouds under contrasting large-scale meteorological conditions, from MCAO to WAA regimes, and highlights the additional role of more local thermodynamic controls, such as temperature inversions. However, these averaged relationships may mask short-lived or localized processes that can strongly modulate cloud phase partitioning and ice growth. Future work should therefore complement this statistical framework with detailed case studies targeting specific mechanisms, such as variations in ice crystal number concentration, changes in ice crystal habits across transition regions, and the influence of aerosol loading on cloud microphysics. Such process-oriented approaches have already proven valuable for identifying the drivers of rapid liquid–ice phase transitions, aerosol-related variability, secondary ice production, and aggregation/riming processes in Arctic mixed-phase clouds (Gayet et al., 2009; Lloyd et al., 2018; Korolev and Lawson, 2026).

https://doi.org/10.5194/egusphere-2026-3265
Preprint. Discussion started: 19 June 2026

6 Summary and conclusion

This study provides a comprehensive characterization of the microphysical and morphological properties of low-level Arctic mixed-phase clouds (MPCs). Representative microphysical properties of MPCs evolving under contrasting meteorological conditions were derived from an analysis of 45 hours of *in situ* airborne measurements collected during four campaigns: ACLOUD, AFLUX, MOSAiC-ACA and HALO-(AC)^3. All flights were conducted in the vicinity of Svalbard and the Greenland Sea. A consistent processing strategy combining multi-sensor measurements and a convolutional neural network-based image classification was used to analyze more than 731,600 ice crystal images across varying synoptic and surface conditions. The main findings are summarized below:

- Four meteorological regimes were identified based on the Marine Cold Air Outbreak index: Marine Cold Air Outbreak (MCAO), Warm Air Advection (WAA), and two transitional states (Norm-C and Norm-W). These conditions are associated with significant differences in thermodynamic and cloud structures. WAA conditions are characterized by strong temperature inversions and relatively warm cloud tops (≈ -3.3 °C), resulting in thin cloud layers dominated by liquid water droplets. By contrast, MCAO regimes exhibit colder cloud tops (≈ -16.5 °C) and well-developed mixed-phase structures with enhanced glaciation and precipitation.

- Under WAA conditions, the liquid phase dominates, with droplet concentrations of 100-150 cm^{-3}, effective diameters exceeding 20 μm, and liquid water content of up to 0.45 g m^{-3} near the cloud top. During MCAOs, mixed-phase characteristics become more pronounced. Median ice water contents reach 0.06 g m^{-3} near the surface, and ice crystal number concentrations of up to 4 L^{-1} near the cloud base suggest efficient riming processes and possibly secondary ice production.

- Temperature inversions also play a role in modulating the vertical structure of mixed-phase clouds. In both MCAO and WAA regimes, stronger inversions are associated with a thinner liquid-containing layer. In WAA conditions, the inversion strength appears to influence the formation and the resilience of the ice phase. Stronger temperature inversions promote favorable conditions for cloud glaciation. By contrast, during MCAOs, strong inversions primarily affect the liquid phase by increasing the liquid water content within the mixed-phase cloud layers. However, their influence on the ice phase is less clearly defined.

- The convolutional neural network-based analysis (Jaffeux et al., 2022) provides a statistical multi-campaign characterization of Arctic ice crystal habits. Rimed particles (CP, RA) prevail during MCAOs, accounting for 50–70 % of the ice mass fraction. This is a signature of active droplet-ice interaction within the mixed-phase layer. Columnar and aggregate shapes (Co, CBC) are frequently observed during WAA in over 80 % of the small-particle population, which points to the prevalence of depositional growth in less turbulent conditions.

- The underlying surface strongly influences the development and microphysics of the cloud. Over the open ocean, clouds are deeper, and the fraction of rimed ice crystals reaches 60–70 % of the ice mass. This shows that stronger surface

https://doi.org/10.5194/egusphere-2026-3265
Preprint. Discussion started: 19 June 2026

turbulent fluxes favor riming and aggregation processes (IWC > 0.05 g m^{-3}; $D_{eff,i}$ > 2000 μm). Over sea ice, under less turbulent conditions, clouds remain shallower, and the fraction of rimed ice particles is significantly lower (30–40 %). Cloud particles are dominated by pristine or weakly aggregated ice crystals. The liquid phase is also more persistent, which is consistent with less consumption of water droplets by riming.

- Surface fluxes and turbulence appear to have a significant influence on the modulation of glaciation and precipitation processes. They suggest that glaciation processes and precipitation efficiency are not independent but are jointly controlled by synoptic forcing and surface type, which together shape the thermodynamic structure of the cloud and its turbulent coupling with the surface.

This study confirms that the microphysical structure of Arctic MPCs is governed by the interplay between synoptic forcing, thermodynamic stability, and surface conditions. Combining multi-campaign *in situ* microphysical observations with morphological ice classification provides a robust basis for evaluating the representation of mixed-phase processes in numerical models. It can also be valuable for assessing the sensitivity of Arctic cloud–precipitation interactions to ongoing surface and climatic changes.

These results also provide valuable insights for developing and improving microphysical parameterizations, particularly with regard to representing riming efficiency, interactions between turbulence and microphysics, and phase partitioning under different thermodynamic conditions. Combining such observations with aerosol measurements could further improve our understanding of glaciation pathways in Arctic mixed-phase clouds and better constrain the role of ice-nucleating particles in shaping the life cycle of boundary layer MPCs. Future work will focus on case studies to investigate in more depth the relationships among turbulence, microphysics, and ice crystal habit to better understand the chain of processes driving phase transitions in low-level Arctic clouds.

Competing interests. At least one of the (co-)authors is a member of the editorial board of Atmospheric Chemistry and Physics.

Author contributions. AD performed the data processing, data selection, analysis of the results and wrote the original manuscript draft. OJ and GM helped AD write the manuscript, provided extensive feedback, and supervised the project. AB contributed to the data processing and to the writing of Section 2 of the manuscript. AC, BD, EV, and JCR provided feedback to improve the first draft of the manuscript. MMos and EJ were involved in the data processing of the cloud probe measurements. JLB, MMon, FS, GP, JD, and OS discussed the results during regular $(MPC)^2$ meetings. MW, AE, CL, EJ, EV, JCR, GP, MMos, JLB, CV and SM provided suggestions to improve the final draft. RD, CG, GM, OJ, MMos, EJ and FMS performed the cloud *in situ* measurements during the airborne campaigns. SM performed the aerosol measurements during the campaigns. AS was responsible for the French *in situ* cloud measurement payload, the Plateforme de Mesures Aéroportées (PMA). SC, MMe, CV, MMos, AE, AH, CL and MW conceived the flight missions.

https://doi.org/10.5194/egusphere-2026-3265
Preprint. Discussion started: 19 June 2026

Acknowledgements. This work was funded by the $(MPC)^2$ project supported by the French Agence Nationale de la Recherche under the grant ANR-22-CE01-0009 and by the Expecting Earth-Care Learning From A-Train (EECLAT, grant 6710) project of the Centre National d'Etudes Spatiales (CNES). Part of this work was funded by the Deutsche Forschungsgemeinschaft (DFG, German Research Foundation) - Project-ID 268020496 - TRR 172 and by project grant no. 316646266 of DFG within the framework of Priority Programme SPP 1294. Part of this work was by the Deutsche Forschungsgemeinschaft (DFG, German Research Foundation) through CRC 301 TPChange (Project ID 428312742) and SPP 1294 HALO (Project ID 316646266). Funding for the operation of the AWI research aircraft Polar 5 and 6 is supported by AWI via grant numbers AWI_PA_02087, AWI_PA_02107, AWI_PA_02112, and AWI_PA_02126.

Data availability. In situ cloud microphysical data (CDP, CAS, 2D-S, CIP, and PIP) from the ACLOUD, AFLUX, MOSAiC-ACA, and HALO-$(AC)^3$ campaigns are freely available from the World Data Center PANGAEA: https://doi.org/10.1594/PANGAEA.940564 (Moser and Voigt, 2022); https://doi.org/10.1594/PANGAEA.940557 (Moser et al., 2022) ; https://doi.org/10.1594/PANGAEA.963247 (Moser et al., 2023a); https://doi.org/10.1594/PANGAEA.899074 (Dupuy et al., 2019); https://doi.org/10.1594/PANGAEA.941498 (Dupuy et al., 2022a); https://doi.org/10.1594/PANGAEA.941538 (Dupuy et al., 2022b); https://doi.org/10.1594/PANGAEA.965734 (Dupuy et al., 2024). The Python code used for CNN-based ice crystal habbit classification is openly available at https://github.com/Ljaffeux/AMT-2022-72 (Jaffeux, 2022). All datasets can be easily accessed, processed, and analyzed using the ac3airborne Python package (https://doi.org/10.5281/zenodo.7305585, Mech et al., 2022b). Aerosol measurements from UHSAS and CPC instruments are available via PANGAEA: https://doi.org/10.1594/PANGAEA.900403 (Mertes et al., 2019); https://doi.org/10.1594/PANGAEA.963771 (Mertes and Wetzel, 2023). ERA5 reanalysis data (**?**) are also available from the CDS: https://cds.climate.copernicus.eu/datasets/reanalysis-era5-single-levels.

https://doi.org/10.5194/egusphere-2026-3265
Preprint. Discussion started: 19 June 2026

References

Achtert, P., O'Connor, E. J., Brooks, I. M., Sotiropoulou, G., Shupe, M. D., Pospichal, B., Brooks, B. J., and Tjernström, M.: Properties of Arctic liquid and mixed-phase clouds from shipborne Cloudnet observations during ACSE 2014, Atmos. Chem. Phys., 20, 14 983–15 002, https://doi.org/10.5194/acp-20-14983-2020, 2020.

Arteaga, D., Planche, C., Tridon, F., Dupuy, R., Baudoux, A., Banson, S., Baray, J.-L., Mioche, G., Ehrlich, A., Mech, M., Mertes, S., Wendisch, M., Wobrock, W., and Jourdan, O.: Arctic mixed-phase clouds simulated by the WRF model: Comparisons with ACLOUD radar and in situ airborne observations and sensitivity of microphysics properties, Atmospheric Research, 307, 107 471, https://doi.org/10.1016/j.atmosres.2024.107471, 2024.

Bailey, M. and Hallett, J.: Growth Rates and Habits of Ice Crystals between -20° and -70°C, J. Atmos. Sci., 61, 514–544, https://doi.org/10.1175/1520-0469(2004)061<0514:GRAHOI>2.0.CO;2, 2004.

Bailey, M. P. and Hallett, J.: A Comprehensive Habit Diagram for Atmospheric Ice Crystals: Confirmation from the Laboratory, AIRS II, and Other Field Studies, Journal of the Atmospheric Sciences, 66, 2888–2899, https://doi.org/10.1175/2009JAS2883.1, 2009.

Baker, B. and Lawson, R. P.: Improvement in Determination of Ice Water Content from Two-Dimensional Particle Imagery. Part I: Image-to-Mass Relationships, Journal of Applied Meteorology and Climatology, 45, 1282–1290, https://doi.org/10.1175/JAM2398.1, 2006.

Baumgardner, D., Jonsson, H., Dawson, W., O'Connor, D., and Newton, R.: The cloud, aerosol and precipitation spectrometer: a new instrument for cloud investigations, Atmospheric Research, 59-60, 251–264, https://doi.org/10.1016/S0169-8095(01)00119-3, 2001.

Baumgardner, D., Abel, S. J., Axisa, D., Cotton, R., Crosier, J., Field, P., Gurganus, C., Heymsfield, A., Korolev, A., Krämer, M., Lawson, P., McFarquhar, G., Ulanowski, Z., and Um, J.: Cloud Ice Properties: In Situ Measurement Challenges, Meteorological Monographs, 58, 9.1–9.23, https://doi.org/10.1175/AMSMONOGRAPHS-D-16-0011.1, 2017.

Bazantay, C., Febvre, G., Jaffeux, L., and Schwarzenboeck, A.: Analysis of Ice Crystal Morphologies in Deep Convective Clouds Using In-Flight Measurements during HAIC–HIWC Cayenne, Journal of the Atmospheric Sciences, 82, 2275–2289, https://doi.org/10.1175/JAS-D-25-0021.1, 2025.

Boisvert, L. N. and Stroeve, J. C.: The Arctic is becoming warmer and wetter as revealed by the Atmospheric Infrared Sounder, Geophysical Research Letters, 42, 4439–4446, https://doi.org/10.1002/2015GL063775, 2015.

Bony, S., Lothon, M., Delanoë, J., Coutris, P., Etienne, J.-C., Aemisegger, F., Albright, A. L., André, T., Bellec, H., Baron, A., Bourdinot, J.-F., Brilouet, P.-E., Bourdon, A., Canonici, J.-C., Caudoux, C., Chazette, P., Cluzeau, M., Cornet, C., Desbios, J.-P., Duchanoy, D., Flamant, C., Fildier, B., Gourbeyre, C., Guiraud, L., Jiang, T., Lainard, C., Le Gac, C., Lendroit, C., Lernould, J., Perrin, T., Pouvesle, F., Richard, P., Rochetin, N., Salaün, K., Schwarzenboeck, A., Seurat, G., Stevens, B., Totems, J., Touzé-Peiffer, L., Vergez, G., Vial, J., Villiger, L., and Vogel, R.: EUREC^4 A observations from the SAFIRE ATR42 aircraft, Earth Syst. Sci. Data, 14, 2021–2064, https://doi.org/10.5194/essd-14-2021-2022, 2022.

Brooks, I. M., Tjernström, M., Persson, P. O. G., Shupe, M. D., Atkinson, R. A., Canut, G., Birch, C. E., Mauritsen, T., Sedlar, J., and Brooks, B. J.: The Turbulent Structure of the Arctic Summer Boundary Layer During The Arctic Summer Cloud-Ocean Study, JGR Atmospheres, 122, 9685–9704, https://doi.org/10.1002/2017jd027234, 2017.

Brown, P. R. A. and Francis, P. N.: Improved Measurements of the Ice Water Content in Cirrus Using a Total-Water Probe, J. Atmos. Oceanic Technol., 12, 410–414, https://doi.org/10.1175/1520-0426(1995)012<0410:IMOTIW>2.0.CO;2, 1995.

Brümmer, B., Rump, B., and Kruspe, G.: A cold air outbreak near Spitsbergen in springtime — Boundary-layer modification and cloud development, Boundary-Layer Meteorol, 61, 13–46, https://doi.org/10.1007/bf02033993, 1992.

https://doi.org/10.5194/egusphere-2026-3265
Preprint. Discussion started: 19 June 2026

Cai, Y., Montague, D. C., Mooiweer-Bryan, W., and Deshler, T.: Performance characteristics of the ultra high sensitivity aerosol spectrometer for particles between 55 and 800nm: Laboratory and field studies, Journal of Aerosol Science, 39, 759–769, https://doi.org/10.1016/j.jaerosci.2008.04.007, 2008.

Cesana, G. V., Pierpaoli, O., Ottaviani, M., Vu, L., Jin, Z., and Silber, I.: The correlation between Arctic sea ice, cloud phase and radiation using A-Train satellites, Atmos. Chem. Phys., 24, 7899–7909, https://doi.org/10.5194/acp-24-7899-2024, 2024.

Chechin, D. G. and Lüpkes, C.: Boundary-Layer Development and Low-level Baroclinicity during High-Latitude Cold-Air Outbreaks: A Simple Model, Boundary-Layer Meteorol, 162, 91–116, https://doi.org/10.1007/s10546-016-0193-2, 2017.

Chechin, D. G., Lüpkes, C., Hartmann, J., Ehrlich, A., and Wendisch, M.: Turbulent structure of the Arctic boundary layer in early summer driven by stability, wind shear and cloud-top radiative cooling: ACLOUD airborne observations, Atmos. Chem. Phys., 23, 4685–4707, https://doi.org/10.5194/acp-23-4685-2023, 2023.

Chellappan, S., Zuidema, P., Kirschler, S., Voigt, C., Cairns, B., Crosbie, E. C., Ferrare, R., Hair, J., Painemal, D., Shingler, T., Shook, M., Thornhill, K. L., Tornow, F., and Sorooshian, A.: Microphysical Evolution in Mixed-Phase Midlatitude Marine Cold-Air Outbreaks, Journal of the Atmospheric Sciences, 81, 1725–1747, https://doi.org/10.1175/JAS-D-23-0203.1, 2024.

Chellini, G. and Kneifel, S.: Turbulence as a Key Driver of Ice Aggregation and Riming in Arctic Low-Level Mixed-Phase Clouds, Revealed by Long-Term Cloud Radar Observations, Geophysical Research Letters, 51, e2023GL106 599, https://doi.org/10.1029/2023GL106599, 2024.

Chellini, G., Gierens, R., and Kneifel, S.: Ice Aggregation in Low-Level Mixed-Phase Clouds at a High Arctic Site: Enhanced by Dendritic Growth and Absent Close to the Melting Level, JGR Atmospheres, 127, e2022JD036 860, https://doi.org/10.1029/2022JD036860, 2022.

Chylik, J., Chechin, D., Dupuy, R., Kulla, B. S., Lüpkes, C., Mertes, S., Mech, M., and Neggers, R. A. J.: Aerosol impacts on the entrainment efficiency of Arctic mixed-phase convection in a simulated air mass over open water, Atmos. Chem. Phys., 23, 4903–4929, https://doi.org/10.5194/acp-23-4903-2023, 2023.

Coopman, Q., Garrett, T. J., Riedi, J., Eckhardt, S., and Stohl, A.: Effects of long-range aerosol transport on the microphysical properties of low-level liquid clouds in the Arctic, Atmos. Chem. Phys., 16, 4661–4674, https://doi.org/10.5194/acp-16-4661-2016, 2016.

Coopman, Q., Riedi, J., Finch, D. P., and Garrett, T. J.: Evidence for Changes in Arctic Cloud Phase Due to Long-Range Pollution Transport, Geophysical Research Letters, 45, https://doi.org/10.1029/2018GL079873, 2018.

Crosier, J., Bower, K. N., Choularton, T. W., Westbrook, C. D., Connolly, P. J., Cui, Z. Q., Crawford, I. P., Capes, G. L., Coe, H., Dorsey, J. R., Williams, P. I., Illingworth, A. J., Gallagher, M. W., and Blyth, A. M.: Observations of ice multiplication in a weakly convective cell embedded in supercooled mid-level stratus, Atmos. Chem. Phys., 11, 257–273, https://doi.org/10.5194/acp-11-257-2011, 2011.

Dada, L., Angot, H., Beck, I., Baccarini, A., Quéléver, L. L. J., Boyer, M., Laurila, T., Brasseur, Z., Jozef, G., De Boer, G., Shupe, M. D., Henning, S., Bucci, S., Dütsch, M., Stohl, A., Petäjä, T., Daellenbach, K. R., Jokinen, T., and Schmale, J.: A central arctic extreme aerosol event triggered by a warm air-mass intrusion, Nat Commun, 13, 5290, https://doi.org/10.1038/s41467-022-32872-2, 2022.

De Boer, G., Eloranta, E. W., and Shupe, M. D.: Arctic Mixed-Phase Stratiform Cloud Properties from Multiple Years of Surface-Based Measurements at Two High-Latitude Locations, Journal of the Atmospheric Sciences, 66, 2874–2887, https://doi.org/10.1175/2009JAS3029.1, 2009.

Defer, E., Pinty, J.-P., Coquillat, S., Martin, J.-M., Prieur, S., Soula, S., Richard, E., Rison, W., Krehbiel, P., Thomas, R., Rodeheffer, D., Vergeiner, C., Malaterre, F., Pedeboy, S., Schulz, W., Farges, T., Gallin, L.-J., Ortéga, P., Ribaud, J.-F., Anderson, G., Betz, H.-D., Meneux, B., Kotroni, V., Lagouvardos, K., Roos, S., Ducrocq, V., Roussot, O., Labatut, L., and Molinié, G.: An overview of the lightning and

https://doi.org/10.5194/egusphere-2026-3265
Preprint. Discussion started: 19 June 2026

atmospheric electricity observations collected in southern France during the HYdrological cycle in Mediterranean EXperiment (HyMeX), Special Observation Period 1, Atmos. Meas. Tech., 8, 649–669, https://doi.org/10.5194/amt-8-649-2015, 2015.

Dezitter, F., Grandin, A., Brenguier, J.-L., Hervy, F., Schlager, H., Villedieu, P., and Zalamansky, G.: HAIC - High Altitude Ice Crystals, in: 5th AIAA Atmospheric and Space Environments Conference, American Institute of Aeronautics and Astronautics, San Diego, CA, https://doi.org/10.2514/6.2013-2674, 2013.

Dong, X., Xi, B., Crosby, K., Long, C. N., Stone, R. S., and Shupe, M. D.: A 10 year climatology of Arctic cloud fraction and radiative forcing at Barrow, Alaska, J. Geophys. Res., 115, 2009JD013 489, https://doi.org/10.1029/2009JD013489, 2010.

Dupuy, R., Jourdan, O., Mioche, G., Gourbeyre, C., Leroy, D., and Schwarzenböck, A.: CDP, CIP and PIP In-situ arctic cloud microphysical properties observed during ACLOUD-AC3 campaign in June 2017, https://doi.org/10.1594/PANGAEA.899074, artwork Size: 68 data points Pages: 68 data points, 2019.

Dupuy, R., Gourbeyre, C., Mioche, G., and Jourdan, O.: French Airborne Measurement Platform (PMA) cloud particle size distribution and volumic cloud particle diffusion properties dataset near Svalbard for AFLUX measurement campaign with POLAR 5 in 2019, https://doi.org/10.1594/PANGAEA.941498, artwork Size: 28 data points Pages: 28 data points, 2022a.

Dupuy, R., Gourbeyre, C., Mioche, G., Moser, M., and Jourdan, O.: French Airborne Measurement Platform (PMA) cloud particle size distribution and volumic cloud particle diffusion properties dataset near Svalbard for MOSAIC-ACA measurement campaign in 2020, https://doi.org/10.1594/PANGAEA.941538, artwork Size: 7 data points Pages: 7 data points, 2022b.

Dupuy, R., Mioche, G., Gourbeyre, C., and Jourdan, O.: French Airborne Measurement Platform (PMA) cloud particle size distribution and volumic cloud particle scattering properties dataset near Svalbard for the HALO-AC3 measurement campaign in 2022, https://doi.org/10.1594/PANGAEA.965734, artwork Size: 12 data points Pages: 12 data points, 2024.

Dziduch, A., Mioche, G., Coopman, Q., Bazantay, C., Delanoë, J., and Jourdan, O.: Regional and seasonal distribution of Arctic low-level cloud types and their relationship to large-scale environmental conditions, Atmos. Chem. Phys., 26, 4019–4047, https://doi.org/10.5194/acp-26-4019-2026, 2026.

D'Alessandro, J. J., Diao, M., Wu, C., Liu, X., Jensen, J. B., and Stephens, B. B.: Cloud Phase and Relative Humidity Distributions over the Southern Ocean in Austral Summer Based on In Situ Observations and CAM5 Simulations, Journal of Climate, 32, 2781–2805, https://doi.org/10.1175/JCLI-D-18-0232.1, 2019.

Ehrlich, A., Wendisch, M., Lüpkes, C., Buschmann, M., Bozem, H., Chechin, D., Clemen, H.-C., Dupuy, R., Eppers, O., Hartmann, J., Herber, A., Jäkel, E., Järvinen, E., Jourdan, O., Kästner, U., Kliesch, L.-L., Köllner, F., Mech, M., Mertes, S., Neuber, R., Ruiz-Donoso, E., Schnaiter, M., Schneider, J., Stapf, J., and Zanatta, M.: A comprehensive in situ and remote sensing data set from the Arctic CLoud Observations Using airborne measurements during polar Day (ACLOUD) campaign, Earth Syst. Sci. Data, 11, 1853–1881, https://doi.org/10.5194/essd-11-1853-2019, 2019.

Ehrlich, A., Crewell, S., Herber, A., Klingebiel, M., Lüpkes, C., Mech, M., Becker, S., Borrmann, S., Bozem, H., Buschmann, M., Clemen, H.-C., De La Torre Castro, E., Dorff, H., Dupuy, R., Eppers, O., Ewald, F., George, G., Giez, A., Grawe, S., Gourbeyre, C., Hartmann, J., Jäkel, E., Joppe, P., Jourdan, O., Jurányi, Z., Kirbus, B., Lucke, J., Luebke, A. E., Maahn, M., Maherndl, N., Mallaun, C., Mayer, J., Mertes, S., Mioche, G., Moser, M., Müller, H., Pörtge, V., Risse, N., Roberts, G., Rosenburg, S., Röttenbacher, J., Schäfer, M., Schaefer, J., Schäfler, A., Schirmacher, I., Schneider, J., Schnitt, S., Stratmann, F., Tatzelt, C., Voigt, C., Walbröl, A., Weber, A., Wetzel, B., Wirth, M., and Wendisch, M.: A comprehensive in situ and remote sensing data set collected during the HALO–$(A\,C)^3$ aircraft campaign, Earth Syst. Sci. Data, 17, 1295–1328, https://doi.org/10.5194/essd-17-1295-2025, 2025.

https://doi.org/10.5194/egusphere-2026-3265
Preprint. Discussion started: 19 June 2026

Field, P. R., Lawson, R. P., Brown, P. R. A., Lloyd, G., Westbrook, C., Moisseev, D., Miltenberger, A., Nenes, A., Blyth, A., Choularton, T., Connolly, P., Buehl, J., Crosier, J., Cui, Z., Dearden, C., DeMott, P., Flossmann, A., Heymsfield, A., Huang, Y., Kalesse, H., Kanji, Z. A., Korolev, A., Kirchgaessner, A., Lasher-Trapp, S., Leisner, T., McFarquhar, G., Phillips, V., Stith, J., and Sullivan, S.: Chapter 7. Secondary Ice Production - current state of the science and recommendations for the future, Meteorological Monographs, pp. AMSMONOGRAPHS–D–16–0014.1, https://doi.org/10.1175/AMSMONOGRAPHS-D-16-0014.1, 2016.

Fletcher, J., Mason, S., and Jakob, C.: The Climatology, Meteorology, and Boundary Layer Structure of Marine Cold Air Outbreaks in Both Hemispheres*, Journal of Climate, 29, 1999–2014, https://doi.org/10.1175/JCLI-D-15-0268.1, 2016.

Gayet, J., Auriol, F., Minikin, A., Ström, J., Seifert, M., Krejci, R., Petzold, A., Febvre, G., and Schumann, U.: Quantitative measurement of the microphysical and optical properties of cirrus clouds with four different in situ probes: Evidence of small ice crystals, Geophysical Research Letters, 29, https://doi.org/10.1029/2001GL014342, 2002.

Gayet, J. F., Crépel, O., Fournol, J. F., and Oshchepkov, S.: A new airborne polar Nephelometer for the measurements of optical and microphysical cloud properties. Part I: Theoretical design, Ann. Geophys., 15, 451–459, https://doi.org/10.1007/s00585-997-0451-1, 1997.

Gayet, J.-F., Mioche, G., Dörnbrack, A., Ehrlich, A., Lampert, A., and Wendisch, M.: Microphysical and optical properties of Arctic mixed-phase clouds. The 9 April 2007 case study., Atmos. Chem. Phys., 9, 6581–6595, https://doi.org/10.5194/acp-9-6581-2009, 2009.

George, G., Luebke, A. E., Klingebiel, M., Mech, M., and Ehrlich, A.: Dropsonde measurements from HALO and POLAR 5 during HALO-(AC)^3 in 2022, https://doi.org/10.1594/PANGAEA.968891, 2024.

Gerber, H., Takano, Y., Garrett, T. J., and Hobbs, P. V.: Nephelometer Measurements of the Asymmetry Parameter, Volume Extinction Coefficient, and Backscatter Ratio in Arctic Clouds, J. Atmos. Sci., 57, 3021–3034, https://doi.org/10.1175/1520-0469(2000)057<3021:NMOTAP>2.0.CO;2, 2000.

Hartmann, J., Gehrmann, M., Kohnert, K., Metzger, S., and Sachs, T.: New calibration procedures for airborne turbulence measurements and accuracy of the methane fluxes during the AirMeth campaigns, Atmos. Meas. Tech., 11, 4567–4581, https://doi.org/10.5194/amt-11-4567-2018, 2018.

Hartmann, M., Gong, X., Kecorius, S., Van Pinxteren, M., Vogl, T., Welti, A., Wex, H., Zeppenfeld, S., Herrmann, H., Wiedensohler, A., and Stratmann, F.: Terrestrial or marine – indications towards the origin of ice-nucleating particles during melt season in the European Arctic up to 83.7° N, Atmos. Chem. Phys., 21, 11 613–11 636, https://doi.org/10.5194/acp-21-11613-2021, 2021.

Hersbach, H., Bell, B., Berrisford, P., Hirahara, S., Horányi, A., Muñoz-Sabater, J., Nicolas, J., Peubey, C., Radu, R., Schepers, D., Simmons, A., Soci, C., Abdalla, S., Abellan, X., Balsamo, G., Bechtold, P., Biavati, G., Bidlot, J., Bonavita, M., Chiara, G., Dahlgren, P., Dee, D., Diamantakis, M., Dragani, R., Flemming, J., Forbes, R., Fuentes, M., Geer, A., Haimberger, L., Healy, S., Hogan, R. J., Hólm, E., Janisková, M., Keeley, S., Laloyaux, P., Lopez, P., Lupu, C., Radnoti, G., Rosnay, P., Rozum, I., Vamborg, F., Villaume, S., and Thépaut, J.: The ERA5 global reanalysis, Q.J.R. Meteorol. Soc., 146, 1999–2049, https://doi.org/10.1002/qj.3803, 2020.

Hirst, E., Kaye, P., Greenaway, R., Field, P., and Johnson, D.: Discrimination of micrometre-sized ice and super-cooled droplets in mixed-phase cloud, Atmospheric Environment, 35, 33–47, https://doi.org/10.1016/S1352-2310(00)00377-0, 2001.

Hofer, S., Hahn, L. C., Shaw, J. K., McGraw, Z. S., Bruno, O., Hellmuth, F., Pietschnig, M., Mostue, I. A., David, R. O., Carlsen, T., and Storelvmo, T.: Realistic representation of mixed-phase clouds increases projected climate warming, Commun Earth Environ, 5, 390, https://doi.org/10.1038/s43247-024-01524-2, 2024.

Hogan, R. J., Tian, L., Brown, P. R. A., Westbrook, C. D., Heymsfield, A. J., and Eastment, J. D.: Radar Scattering from Ice Aggregates Using the Horizontally Aligned Oblate Spheroid Approximation, Journal of Applied Meteorology and Climatology, 51, 655–671, https://doi.org/10.1175/JAMC-D-11-074.1, 2012.

https://doi.org/10.5194/egusphere-2026-3265
Preprint. Discussion started: 19 June 2026

Intrieri, J. M., Shupe, M. D., Uttal, T., and McCarty, B. J.: An annual cycle of Arctic cloud characteristics observed by radar and lidar at SHEBA, J. Geophys. Res., 107, https://doi.org/10.1029/2000JC000423, 2002.

Irish, V. E., Hanna, S. J., Willis, M. D., China, S., Thomas, J. L., Wentzell, J. J. B., Cirisan, A., Si, M., Leaitch, W. R., Murphy, J. G., Abbatt, J. P. D., Laskin, A., Girard, E., and Bertram, A. K.: Ice nucleating particles in the marine boundary layer in the Canadian Arctic during summer 2014, Atmos. Chem. Phys., 19, 1027–1039, https://doi.org/10.5194/acp-19-1027-2019, 2019.

Jackson, R. C., McFarquhar, G. M., Korolev, A. V., Earle, M. E., Liu, P. S. K., Lawson, R. P., Brooks, S., Wolde, M., Laskin, A., and Freer, M.: The dependence of ice microphysics on aerosol concentration in arctic mixed-phase stratus clouds during ISDAC and M-PACE: AEROSOL EFFECTS ON ARCTIC STRATUS, J. Geophys. Res., 117, n/a–n/a, https://doi.org/10.1029/2012JD017668, 2012.

Jaffeux, L.: LJaffeux/AMT-2022-72: Ice crystals images from Optical Array Probes: classification with Convolutional Neural Networks, https://doi.org/10.5281/ZENODO.6912294, 2022.

Jaffeux, L., Schwarzenböck, A., Coutris, P., and Duroure, C.: Ice crystal images from optical array probes: classification with convolutional neural networks, Atmos. Meas. Tech., 15, 5141–5157, https://doi.org/10.5194/amt-15-5141-2022, 2022.

Jourdan, O., Mioche, G., Garrett, T. J., Schwarzenböck, A., Vidot, J., Xie, Y., Shcherbakov, V., Yang, P., and Gayet, J.: Coupling of the microphysical and optical properties of an Arctic nimbostratus cloud during the ASTAR 2004 experiment: Implications for light-scattering modeling, J. Geophys. Res., 115, 2010JD014 016, https://doi.org/10.1029/2010JD014016, 2010.

Järvinen, E., Nehlert, F., Xu, G., Waitz, F., Mioche, G., Dupuy, R., Jourdan, O., and Schnaiter, M.: Investigating the vertical extent and short-wave radiative effects of the ice phase in Arctic summertime low-level clouds, Atmos. Chem. Phys., 23, 7611–7633, https://doi.org/10.5194/acp-23-7611-2023, 2023.

Kanji, Z. A., Ladino, L. A., Wex, H., Boose, Y., Burkert-Kohn, M., Cziczo, D. J., and Krämer, M.: Overview of Ice Nucleating Particles, Meteorological Monographs, 58, 1.1–1.33, https://doi.org/10.1175/AMSMONOGRAPHS-D-16-0006.1, 2017.

Kay, J. E., L'Ecuyer, T., Chepfer, H., Loeb, N., Morrison, A., and Cesana, G.: Recent Advances in Arctic Cloud and Climate Research, Curr Clim Change Rep, 2, 159–169, https://doi.org/10.1007/s40641-016-0051-9, 2016.

Knudsen, E. M., Heinold, B., Dahlke, S., Bozem, H., Crewell, S., Gorodetskaya, I. V., Heygster, G., Kunkel, D., Maturilli, M., Mech, M., Viceto, C., Rinke, A., Schmithüsen, H., Ehrlich, A., Macke, A., Lüpkes, C., and Wendisch, M.: Meteorological conditions during the ACLOUD/PASCAL field campaign near Svalbard in early summer 2017, Atmos. Chem. Phys., 18, 17 995–18 022, https://doi.org/10.5194/acp-18-17995-2018, 2018.

Kolstad, E. W., Bracegirdle, T. J., and Seierstad, I. A.: Marine cold-air outbreaks in the North Atlantic: temporal distribution and associations with large-scale atmospheric circulation, Clim Dyn, 33, 187–197, https://doi.org/10.1007/s00382-008-0431-5, 2009.

Korolev, A., McFarquhar, G., Field, P. R., Franklin, C., Lawson, P., Wang, Z., Williams, E., Abel, S. J., Axisa, D., Borrmann, S., Crosier, J., Fugal, J., Krämer, M., Lohmann, U., Schlenczek, O., Schnaiter, M., and Wendisch, M.: Mixed-Phase Clouds: Progress and Challenges, Meteorological Monographs, 58, 5.1–5.50, https://doi.org/10.1175/AMSMONOGRAPHS-D-17-0001.1, 2017.

Korolev, A. V. and Lawson, R. P.: Microphysics of Arctic Stratiform Boundary-layer Clouds during ARCSIX, Atmos. Chem. Phys., 26, 2331–2352, https://doi.org/10.5194/acp-26-2331-2026, 2026.

Korolev, A. V., Emery, E. F., Strapp, J. W., Cober, S. G., Isaac, G. A., Wasey, M., and Marcotte, D.: Small Ice Particles in Tropospheric Clouds: Fact or Artifact? Airborne Icing Instrumentation Evaluation Experiment, Bulletin of the American Meteorological Society, 92, 967–973, https://doi.org/10.1175/2010BAMS3141.1, 2011.

https://doi.org/10.5194/egusphere-2026-3265
Preprint. Discussion started: 19 June 2026

Lackner, C. P., Geerts, B., Juliano, T. W., Xue, L., and Kosovic, B.: Vertical Structure of Clouds and Precipitation During Arctic Cold-Air Outbreaks and Warm-Air Intrusions: Observations From COMBLE, JGR Atmospheres, 128, e2022JD038 403, https://doi.org/10.1029/2022JD038403, 2023.

Lance, S., Brock, C. A., Rogers, D., and Gordon, J. A.: Water droplet calibration of the Cloud Droplet Probe (CDP) and in-flight performance in liquid, ice and mixed-phase clouds during ARCPAC, Atmos. Meas. Tech., 3, 1683–1706, https://doi.org/10.5194/amt-3-1683-2010, 2010.

Lang, A., Yang, S., and Kaas, E.: Sea ice thickness and recent Arctic warming, Geophysical Research Letters, 44, 409–418, https://doi.org/10.1002/2016GL071274, 2017.

Lawson, R. P., O'Connor, D., Zmarzly, P., Weaver, K., Baker, B., Mo, Q., and Jonsson, H.: The 2D-S (Stereo) Probe: Design and Preliminary Tests of a New Airborne, High-Speed, High-Resolution Particle Imaging Probe, Journal of Atmospheric and Oceanic Technology, 23, 1462–1477, https://doi.org/10.1175/JTECH1927.1, 2006.

Leroy, D., Fontaine, E., Schwarzenboeck, A., and Strapp, J. W.: Ice Crystal Sizes in High Ice Water Content Clouds. Part I: On the Computation of Median Mass Diameter from In Situ Measurements, Journal of Atmospheric and Oceanic Technology, 33, 2461–2476, https://doi.org/10.1175/JTECH-D-15-0151.1, 2016.

Lloyd, G., Choularton, T. W., Bower, K. N., Crosier, J., Jones, H., Dorsey, J. R., Gallagher, M. W., Connolly, P., Kirchgaessner, A. C. R., and Lachlan-Cope, T.: Observations and comparisons of cloud microphysical properties in spring and summertime Arctic stratocumulus clouds during the ACCACIA campaign, Atmos. Chem. Phys., 15, 3719–3737, https://doi.org/10.5194/acp-15-3719-2015, 2015.

Lloyd, G., Choularton, T. W., Bower, K. N., Gallagher, M. W., Crosier, J., O'Shea, S., Abel, S. J., Fox, S., Cotton, R., and Boutle, I. A.: In situ measurements of cloud microphysical and aerosol properties during the break-up of stratocumulus cloud layers in cold air outbreaks over the North Atlantic, Atmos. Chem. Phys., 18, 17 191–17 206, https://doi.org/10.5194/acp-18-17191-2018, 2018.

Maherndl, N., Moser, M., Schirmacher, I., Bansemer, A., Lucke, J., Voigt, C., and Maahn, M.: How does riming influence the observed spatial variability of ice water in mixed-phase clouds?, Atmos. Chem. Phys., 24, 13 935–13 960, https://doi.org/10.5194/acp-24-13935-2024, 2024.

McFarquhar, G. M., Zhang, G., Poellot, M. R., Kok, G. L., McCoy, R., Tooman, T., Fridlind, A., and Heymsfield, A. J.: Ice properties of single-layer stratocumulus during the Mixed-Phase Arctic Cloud Experiment: 1. Observations, J. Geophys. Res., 112, 2007JD008 633, https://doi.org/10.1029/2007JD008633, 2007.

McIlhattan, E. A., L'Ecuyer, T. S., and Miller, N. B.: Observational Evidence Linking Arctic Supercooled Liquid Cloud Biases in CESM to Snowfall Processes, J. Climate, 30, 4477–4495, https://doi.org/10.1175/JCLI-D-16-0666.1, 2017.

Mech, M., Ehrlich, A., Herber, A., Lüpkes, C., Wendisch, M., Becker, S., Boose, Y., Chechin, D., Crewell, S., Dupuy, R., Gourbeyre, C., Hartmann, J., Jäkel, E., Jourdan, O., Kliesch, L.-L., Klingebiel, M., Kulla, B. S., Mioche, G., Moser, M., Risse, N., Ruiz-Donoso, E., Schäfer, M., Stapf, J., and Voigt, C.: MOSAiC-ACA and AFLUX - Arctic airborne campaigns characterizing the exit area of MOSAiC, Sci Data, 9, 790, https://doi.org/10.1038/s41597-022-01900-7, 2022a.

Mech, M., Risse, N., Marrollo, G., and Paul, D.: ac3airborne, https://doi.org/10.5281/ZENODO.7305585, 2022b.

Mertes, S. and Wetzel, B.: Airborne in-situ measurements of aerosol properties of cloud particle residuals / ambient particles and of the cloud water content / water vapor during the HALO-AC3 campaign in March and April 2022, https://doi.org/10.1594/PANGAEA.963771, artwork Size: 13 datasets Medium: application/zip Pages: 13 datasets, 2023.

https://doi.org/10.5194/egusphere-2026-3265
Preprint. Discussion started: 19 June 2026

Mertes, S., Schröder, F., and Wiedensohler, A.: The Particle Detection Efficiency Curve of the TSI-3010 CPC as a Function of the Temperature Difference between Saturator and Condenser, Aerosol Science and Technology, 23, 257–261, https://doi.org/10.1080/02786829508965310, 1995.

Mertes, S., Kästner, U., and Macke, A.: Airborne in-situ measurements of the aerosol absorption coefficient, aerosol particle number concentration and size distribution of cloud particle residuals and ambient aerosol particles during the ACLOUD campaign in May and June 2017, https://doi.org/10.1594/PANGAEA.900403, artwork Size: 19 datasets Medium: application/zip Pages: 19 datasets, 2019.

Michaelis, J., Schmitt, A. U., Lüpkes, C., Hartmann, J., Birnbaum, G., and Vihma, T.: Observations of marine cold-air outbreaks: a comprehensive data set of airborne and dropsonde measurements from the Springtime Atmospheric Boundary Layer Experiment (STABLE), Earth Syst. Sci. Data, 14, 1621–1637, https://doi.org/10.5194/essd-14-1621-2022, 2022.

Mioche, G. and Jourdan, O.: Spaceborne Remote Sensing and Airborne In Situ Observations of Arctic Mixed-Phase Clouds, in: Mixed-Phase Clouds, pp. 121–150, Elsevier, ISBN 978-0-12-810549-8, https://doi.org/10.1016/B978-0-12-810549-8.00006-4, 2018.

Mioche, G., Jourdan, O., Delanoë, J., Gourbeyre, C., Febvre, G., Dupuy, R., Monier, M., Szczap, F., Schwarzenboeck, A., and Gayet, J.-F.: Vertical distribution of microphysical properties of Arctic springtime low-level mixed-phase clouds over the Greenland and Norwegian seas, Atmos. Chem. Phys., 17, 12 845–12 869, https://doi.org/10.5194/acp-17-12845-2017, 2017.

Morrison, H., de Boer, G., Feingold, G., Harrington, J., Shupe, M. D., and Sulia, K.: Resilience of persistent Arctic mixed-phase clouds, Nature Geosci, 5, 11–17, https://doi.org/10.1038/ngeo1332, 2012.

Moser, M. and Voigt, C.: DLR in-situ cloud measurements during AFLUX Arctic airborne campaign, https://doi.org/10.1594/PANGAEA.940564, artwork Size: 52 data points Pages: 52 data points, 2022.

Moser, M., Voigt, C., and Hahn, V.: DLR in-situ cloud measurements during MOSAiC-ACA Arctic airborne campaign, https://doi.org/10.1594/PANGAEA.940557, artwork Size: 40 data points Pages: 40 data points, 2022.

Moser, M., Lucke, J., De La Torre Castro, E., Mayer, J., and Voigt, C.: DLR in situ cloud measurements during HALO-(AC)^3 Arctic airborne campaign, https://doi.org/10.1594/PANGAEA.963247, artwork Size: 52 data points Pages: 52 data points, 2023a.

Moser, M., Voigt, C., Jurkat-Witschas, T., Hahn, V., Mioche, G., Jourdan, O., Dupuy, R., Gourbeyre, C., Schwarzenboeck, A., Lucke, J., Boose, Y., Mech, M., Borrmann, S., Ehrlich, A., Herber, A., Lüpkes, C., and Wendisch, M.: Microphysical and thermodynamic phase analyses of Arctic low-level clouds measured above the sea ice and the open ocean in spring and summer, Atmos. Chem. Phys., 23, 7257–7280, https://doi.org/10.5194/acp-23-7257-2023, 2023b.

Moser, M., Voigt, C., Eppers, O., Lucke, J., De La Torre Castro, E., Mayer, J., Dupuy, R., Mioche, G., Jourdan, O., Clemen, H.-C., Schneider, J., Joppe, P., Mertes, S., Wetzel, B., Borrmann, S., Klingebiel, M., Mech, M., Lüpkes, C., Crewell, S., Ehrlich, A., Herber, A., and Wendisch, M.: The Arctic Low-Level Mixed-Phase Haze Regime and its Microphysical Differences to Mixed-Phase Clouds, https://doi.org/10.5194/egusphere-2025-3876, 2025.

Mroz, K., Dhillon, R., and Battaglia, A.: Unveiling Cloud Microphysics of Marine Cold Air Outbreaks Through A-Train's Active Instrumentation, Atmosphere, 16, 518, https://doi.org/10.3390/atmos16050518, 2025.

Nakaya, U.: Snow Crystals: Natural and Artificial, Harvard University Press, ISBN 978-0-674-18276-9, https://doi.org/10.4159/harvard.9780674182769, 1954.

Niederdrenk, A. L. and Notz, D.: Arctic Sea Ice in a 1.5°C Warmer World, Geophysical Research Letters, 45, 1963–1971, https://doi.org/10.1002/2017GL076159, 2018.

Nygård, T., Valkonen, T., and Vihma, T.: Characteristics of Arctic low-tropospheric humidity inversions based on radio soundings, Atmos. Chem. Phys., 14, 1959–1971, https://doi.org/10.5194/acp-14-1959-2014, 2014.

https://doi.org/10.5194/egusphere-2026-3265
Preprint. Discussion started: 19 June 2026

Papritz, L. and Spengler, T.: A Lagrangian Climatology of Wintertime Cold Air Outbreaks in the Irminger and Nordic Seas and Their Role in Shaping Air–Sea Heat Fluxes, J. Climate, 30, 2717–2737, https://doi.org/10.1175/JCLI-D-16-0605.1, 2017.

Park, H.-S., Lee, S., Son, S.-W., Feldstein, S. B., and Kosaka, Y.: The Impact of Poleward Moisture and Sensible Heat Flux on Arctic Winter Sea Ice Variability*, Journal of Climate, 28, 5030–5040, https://doi.org/10.1175/JCLI-D-15-0074.1, 2015.

Pasquier, J. T., Henneberger, J., Ramelli, F., Lauber, A., David, R. O., Wieder, J., Carlsen, T., Gierens, R., Maturilli, M., and Lohmann, U.: Conditions favorable for secondary ice production in Arctic mixed-phase clouds, Atmos. Chem. Phys., 22, 15 579–15 601, https://doi.org/10.5194/acp-22-15579-2022, 2022.

Phillips, V. T. J., Formenton, M., Bansemer, A., Kudzotsa, I., and Lienert, B.: A Parameterization of Sticking Efficiency for Collisions of Snow and Graupel with Ice Crystals: Theory and Comparison with Observations*, Journal of the Atmospheric Sciences, 72, 4885–4902, https://doi.org/10.1175/JAS-D-14-0096.1, 2015.

Pithan, F., Medeiros, B., and Mauritsen, T.: Mixed-phase clouds cause climate model biases in Arctic wintertime temperature inversions, Clim Dyn, 43, 289–303, https://doi.org/10.1007/s00382-013-1964-9, 2014.

Pithan, F., Svensson, G., Caballero, R., Chechin, D., Cronin, T. W., Ekman, A. M. L., Neggers, R., Shupe, M. D., Solomon, A., Tjernström, M., and Wendisch, M.: Role of air-mass transformations in exchange between the Arctic and mid-latitudes, Nature Geosci, 11, 805–812, https://doi.org/10.1038/s41561-018-0234-1, 2018.

Raatikainen, T., Calderón, S., Järvinen, E., Prank, M., and Romakkaniemi, S.: Can rime splintering explain the ice production in Arctic mixed-phase clouds?, Atmos. Chem. Phys., 26, 5019–5038, https://doi.org/10.5194/acp-26-5019-2026, 2026.

Raif, E. N., Barr, S. L., Tarn, M. D., McQuaid, J. B., Daily, M. I., Abel, S. J., Barrett, P. A., Bower, K. N., Field, P. R., Carslaw, K. S., and Murray, B. J.: High ice-nucleating particle concentrations associated with Arctic haze in springtime cold-air outbreaks, Atmos. Chem. Phys., 24, 14 045–14 072, https://doi.org/10.5194/acp-24-14045-2024, 2024.

Raillard, L., Vignon, , Rivière, G., Madeleine, J., Meurdesoif, Y., Delanoë, J., Caubel, A., Jourdan, O., Baudoux, A., Fromang, S., and Conesa, P.: Leveraging RALI-THINICE Observations to Assess How the ICOLMDZ Model Simulates Clouds Embedded in Arctic Cyclones, JGR Atmospheres, 129, e2024JD040 973, https://doi.org/10.1029/2024JD040973, 2024.

Rantanen, M., Karpechko, A. Y., Lipponen, A., Nordling, K., Hyvärinen, O., Ruosteenoja, K., Vihma, T., and Laaksonen, A.: The Arctic has warmed nearly four times faster than the globe since 1979, Commun Earth Environ, 3, 168, https://doi.org/10.1038/s43247-022-00498-3, 2022.

Rinaldi, M., Hiranuma, N., Santachiara, G., Mazzola, M., Mansour, K., Paglione, M., Rodriguez, C. A., Traversi, R., Becagli, S., Cappelletti, D., and Belosi, F.: Ice-nucleating particle concentration measurements from Ny-Ålesund during the Arctic spring–summer in 2018, Atmos. Chem. Phys., 21, 14 725–14 748, https://doi.org/10.5194/acp-21-14725-2021, 2021.

Sanchez, K. J., Zhang, B., Liu, H., Brown, M. D., Crosbie, E. C., Gallo, F., Hair, J. W., Hostetler, C. A., Jordan, C. E., Robinson, C. E., Scarino, A. J., Shingler, T. J., Shook, M. A., Thornhill, K. L., Wiggins, E. B., Winstead, E. L., Ziemba, L. D., Saliba, G., Lewis, S. L., Russell, L. M., Quinn, P. K., Bates, T. S., Porter, J., Bell, T. G., Gaube, P., Saltzman, E. S., Behrenfeld, M. J., and Moore, R. H.: North Atlantic Ocean SST-gradient-driven variations in aerosol and cloud evolution along Lagrangian cold-air outbreak trajectories, Atmos. Chem. Phys., 22, 2795–2815, https://doi.org/10.5194/acp-22-2795-2022, 2022.

Schirmacher, I., Kollias, P., Lamer, K., Mech, M., Pfitzenmaier, L., Wendisch, M., and Crewell, S.: Assessing Arctic low-level clouds and precipitation from above – a radar perspective, Atmos. Meas. Tech., 16, 4081–4100, https://doi.org/10.5194/amt-16-4081-2023, 2023.

https://doi.org/10.5194/egusphere-2026-3265
Preprint. Discussion started: 19 June 2026

Schirmacher, I., Schnitt, S., Klingebiel, M., Maherndl, N., Kirbus, B., Ehrlich, A., Mech, M., and Crewell, S.: Clouds and precipitation in the initial phase of marine cold-air outbreaks as observed by airborne remote sensing, Atmos. Chem. Phys., 24, 12 823–12 842, https://doi.org/10.5194/acp-24-12823-2024, 2024.

Serreze, M. C. and Francis, J. A.: The Arctic Amplification Debate, Climatic Change, 76, 241–264, https://doi.org/10.1007/s10584-005-9017-y, 2006.

Shupe, M. D., Uttal, T., and Matrosov, S. Y.: Arctic Cloud Microphysics Retrievals from Surface-Based Remote Sensors at SHEBA, Journal of Applied Meteorology, 44, 1544–1562, https://doi.org/10.1175/JAM2297.1, 2005.

Shupe, M. D., Matrosov, S. Y., and Uttal, T.: Arctic Mixed-Phase Cloud Properties Derived from Surface-Based Sensors at SHEBA, Journal of the Atmospheric Sciences, 63, 697–711, https://doi.org/10.1175/JAS3659.1, 2006.

Shupe, M. D., Kollias, P., Persson, P. O. G., and McFarquhar, G. M.: Vertical Motions in Arctic Mixed-Phase Stratiform Clouds, Journal of the Atmospheric Sciences, 65, 1304–1322, https://doi.org/10.1175/2007JAS2479.1, 2008.

Shupe, M. D., Walden, V. P., Eloranta, E., Uttal, T., Campbell, J. R., Starkweather, S. M., and Shiobara, M.: Clouds at Arctic Atmospheric Observatories. Part I: Occurrence and Macrophysical Properties, Journal of Applied Meteorology and Climatology, 50, 626–644, https://doi.org/10.1175/2010JAMC2467.1, 2011.

Shupe, M. D., Rex, M., Blomquist, B., Persson, P. O. G., Schmale, J., Uttal, T., Althausen, D., Angot, H., Archer, S., Bariteau, L., Beck, I., Bilberry, J., Bucci, S., Buck, C., Boyer, M., Brasseur, Z., Brooks, I. M., Calmer, R., Cassano, J., Castro, V., Chu, D., Costa, D., Cox, C. J., Creamean, J., Crewell, S., Dahlke, S., Damm, E., De Boer, G., Deckelmann, H., Dethloff, K., Dütsch, M., Ebell, K., Ehrlich, A., Ellis, J., Engelmann, R., Fong, A. A., Frey, M. M., Gallagher, M. R., Ganzeveld, L., Gradinger, R., Graeser, J., Greenamyer, V., Griesche, H., Griffiths, S., Hamilton, J., Heinemann, G., Helmig, D., Herber, A., Heuzé, C., Hofer, J., Houchens, T., Howard, D., Inoue, J., Jacobi, H.-W., Jaiser, R., Jokinen, T., Jourdan, O., Jozef, G., King, W., Kirchgaessner, A., Klingebiel, M., Krassovski, M., Krumpen, T., Lampert, A., Landing, W., Laurila, T., Lawrence, D., Lonardi, M., Loose, B., Lüpkes, C., Maahn, M., Macke, A., Maslowski, W., Marsay, C., Maturilli, M., Mech, M., Morris, S., Moser, M., Nicolaus, M., Ortega, P., Osborn, J., Pätzold, F., Perovich, D. K., Petäjä, T., Pilz, C., Pirazzini, R., Posman, K., Powers, H., Pratt, K. A., Preußer, A., Quéléver, L., Radenz, M., Rabe, B., Rinke, A., Sachs, T., Schulz, A., Siebert, H., Silva, T., Solomon, A., Sommerfeld, A., Spreen, G., Stephens, M., Stohl, A., Svensson, G., Uin, J., Viegas, J., Voigt, C., Von Der Gathen, P., Wehner, B., Welker, J. M., Wendisch, M., Werner, M., Xie, Z., and Yue, F.: Overview of the MOSAiC expedition: Atmosphere, Elem Sci Anth, 10, 00 060, https://doi.org/10.1525/elementa.2021.00060, 2022.

Slättberg, N., Dahlke, S., and Maturilli, M.: Fram Strait Marine Cold Air Outbreaks in CARRA and ERA5: Effects on Surface Turbulent Heat Fluxes and the Vertical Structure of the Troposphere, JGR Atmospheres, 130, https://doi.org/10.1029/2024jd042908, 2025.

Sotiropoulou, G., Sedlar, J., Tjernström, M., Shupe, M. D., Brooks, I. M., and Persson, P. O. G.: The thermodynamic structure of summer Arctic stratocumulus and the dynamic coupling to the surface, Atmos. Chem. Phys., 14, 12 573–12 592, https://doi.org/10.5194/acp-14-12573-2014, 2014.

Spreen, G., Kaleschke, L., and Heygster, G.: Sea ice remote sensing using AMSR-E 89-GHz channels, J. Geophys. Res., 113, C02S03, https://doi.org/10.1029/2005JC003384, 2008.

Tan, I. and Storelvmo, T.: Evidence of Strong Contributions From Mixed-Phase Clouds to Arctic Climate Change, Geophysical Research Letters, 46, 2894–2902, https://doi.org/10.1029/2018GL081871, 2019.

Tjernström, M., Sedlar, J., and Shupe, M. D.: How Well Do Regional Climate Models Reproduce Radiation and Clouds in the Arctic? An Evaluation of ARCMIP Simulations, Journal of Applied Meteorology and Climatology, 47, 2405–2422, https://doi.org/10.1175/2008JAMC1845.1, 2008.

https://doi.org/10.5194/egusphere-2026-3265
Preprint. Discussion started: 19 June 2026

Tjernström, M., Leck, C., Birch, C. E., Bottenheim, J. W., Brooks, B. J., Brooks, I. M., Bäcklin, L., Chang, R. Y.-W., De Leeuw, G., Di Liberto, L., De La Rosa, S., Granath, E., Graus, M., Hansel, A., Heintzenberg, J., Held, A., Hind, A., Johnston, P., Knulst, J., Martin, M., Matrai, P. A., Mauritsen, T., Müller, M., Norris, S. J., Orellana, M. V., Orsini, D. A., Paatero, J., Persson, P. O. G., Gao, Q., Rauschenberg, C., Ristovski, Z., Sedlar, J., Shupe, M. D., Sierau, B., Sirevaag, A., Sjogren, S., Stetzer, O., Swietlicki, E., Szczodrak, M., Vaattovaara, P., Wahlberg, N., Westberg, M., and Wheeler, C. R.: The Arctic Summer Cloud Ocean Study (ASCOS): overview and experimental design, Atmos. Chem. Phys., 14, 2823–2869, https://doi.org/10.5194/acp-14-2823-2014, 2014.

Verlinde, J., Harrington, J. Y., McFarquhar, G. M., Yannuzzi, V. T., Avramov, A., Greenberg, S., Johnson, N., Zhang, G., Poellot, M. R., Mather, J. H., Turner, D. D., Eloranta, E. W., Zak, B. D., Prenni, A. J., Daniel, J. S., Kok, G. L., Tobin, D. C., Holz, R., Sassen, K., Spangenberg, D., Minnis, P., Tooman, T. P., Ivey, M. D., Richardson, S. J., Bahrmann, C. P., Shupe, M., DeMott, P. J., Heymsfield, A. J., and Schofield, R.: The Mixed-Phase Arctic Cloud Experiment, Bull. Amer. Meteor. Soc., 88, 205–222, https://doi.org/10.1175/BAMS-88-2-205, 2007.

Waitz, F., Schnaiter, M., Leisner, T., and Järvinen, E.: In situ observation of riming in mixed-phase clouds using the PHIPS probe, Atmos. Chem. Phys., 22, 7087–7103, https://doi.org/10.5194/acp-22-7087-2022, 2022.

Walbröl, A., Michaelis, J., Becker, S., Dorff, H., Ebell, K., Gorodetskaya, I., Heinold, B., Kirbus, B., Lauer, M., Maherndl, N., Maturilli, M., Mayer, J., Müller, H., Neggers, R. A. J., Paulus, F. M., Röttenbacher, J., Rückert, J. E., Schirmacher, I., Slättberg, N., Ehrlich, A., Wendisch, M., and Crewell, S.: Contrasting extremely warm and long-lasting cold air anomalies in the North Atlantic sector of the Arctic during the HALO-$(A\ C)^3$ campaign, Atmos. Chem. Phys., 24, 8007–8029, https://doi.org/10.5194/acp-24-8007-2024, 2024.

Wallentin, G., Ickes, L., Achtert, P., Tesche, M., and Hoose, C.: The prevalence of Arctic multilayer clouds and their observed and modelled characteristics, Atmos. Chem. Phys., 26, 3069–3089, https://doi.org/10.5194/acp-26-3069-2026, 2026.

Wendisch, M., ed.: Airborne measurements for environmental research: methods and instruments, Wiley series in atmospheric physics and remote sensing, Wiley-VCH, Weinheim, ISBN 978-3-527-65323-2 978-3-527-40996-9, 2013.

Wendisch, M., Macke, A., Ehrlich, A., Lüpkes, C., Mech, M., Chechin, D., Dethloff, K., Velasco, C. B., Bozem, H., Brückner, M., Clemen, H.-C., Crewell, S., Donth, T., Dupuy, R., Ebell, K., Egerer, U., Engelmann, R., Engler, C., Eppers, O., Gehrmann, M., Gong, X., Gottschalk, M., Gourbeyre, C., Griesche, H., Hartmann, J., Hartmann, M., Heinold, B., Herber, A., Herrmann, H., Heygster, G., Hoor, P., Jafariserajehlou, S., Jäkel, E., Järvinen, E., Jourdan, O., Kästner, U., Kecorius, S., Knudsen, E. M., Köllner, F., Kretzschmar, J., Lelli, L., Leroy, D., Maturilli, M., Mei, L., Mertes, S., Mioche, G., Neuber, R., Nicolaus, M., Nomokonova, T., Notholt, J., Palm, M., Van Pinxteren, M., Quaas, J., Richter, P., Ruiz-Donoso, E., Schäfer, M., Schmieder, K., Schnaiter, M., Schneider, J., Schwarzenböck, A., Seifert, P., Shupe, M. D., Siebert, H., Spreen, G., Stapf, J., Stratmann, F., Vogl, T., Welti, A., Wex, H., Wiedensohler, A., Zanatta, M., and Zeppenfeld, S.: The Arctic Cloud Puzzle: Using ACLOUD/PASCAL Multiplatform Observations to Unravel the Role of Clouds and Aerosol Particles in Arctic Amplification, Bulletin of the American Meteorological Society, 100, 841–871, https://doi.org/10.1175/BAMS-D-18-0072.1, 2019.

Wendisch, M., Brückner, M., Crewell, S., Ehrlich, A., Notholt, J., Lüpkes, C., Macke, A., Burrows, J. P., Rinke, A., Quaas, J., Maturilli, M., Schemann, V., Shupe, M. D., Akansu, E. F., Barrientos-Velasco, C., Bärfuss, K., Blechschmidt, A.-M., Block, K., Bougoudis, I., Bozem, H., Böckmann, C., Bracher, A., Bresson, H., Bretschneider, L., Buschmann, M., Chechin, D. G., Chylik, J., Dahlke, S., Deneke, H., Dethloff, K., Donth, T., Dorn, W., Dupuy, R., Ebell, K., Egerer, U., Engelmann, R., Eppers, O., Gerdes, R., Gierens, R., Gorodetskaya, I. V., Gottschalk, M., Griesche, H., Gryanik, V. M., Handorf, D., Harm-Altstädter, B., Hartmann, J., Hartmann, M., Heinold, B., Herber, A., Herrmann, H., Heygster, G., Höschel, I., Hofmann, Z., Hölemann, J., Hünerbein, A., Jafariserajehlou, S., Jäkel, E., Jacobi, C., Janout, M., Jansen, F., Jourdan, O., Jurányi, Z., Kalesse-Los, H., Kanzow, T., Käthner, R., Kliesch, L. L., Klingebiel, M., Knudsen, E. M., Kovács,

https://doi.org/10.5194/egusphere-2026-3265
Preprint. Discussion started: 19 June 2026

T., Körtke, W., Krampe, D., Kretzschmar, J., Kreyling, D., Kulla, B., Kunkel, D., Lampert, A., Lauer, M., Lelli, L., Von Lerber, A., Linke, O., Löhnert, U., Lonardi, M., Losa, S. N., Losch, M., Maahn, M., Mech, M., Mei, L., Mertes, S., Metzner, E., Mewes, D., Michaelis, J., Mioche, G., Moser, M., Nakoudi, K., Neggers, R., Neuber, R., Nomokonova, T., Oelker, J., Papakonstantinou-Presvelou, I., Pätzold, F., Pefanis, V., Pohl, C., Van Pinxteren, M., Radovan, A., Rhein, M., Rex, M., Richter, A., Risse, N., Ritter, C., Rostosky, P., Rozanov, V. V., Donoso, E. R., Saavedra Garfias, P., Salzmann, M., Schacht, J., Schäfer, M., Schneider, J., Schnierstein, N., Seifert, P., Seo, S., Siebert, H., Soppa, M. A., Spreen, G., Stachlewska, I. S., Stapf, J., Stratmann, F., Tegen, I., Viceto, C., Voigt, C., Vountas, M., Walbröl, A., Walter, M., Wehner, B., Wex, H., Willmes, S., Zanatta, M., and Zeppenfeld, S.: Atmospheric and Surface Processes, and Feedback Mechanisms Determining Arctic Amplification: A Review of First Results and Prospects of the (AC)3 Project, Bulletin of the American Meteorological Society, 104, E208–E242, https://doi.org/10.1175/BAMS-D-21-0218.1, 2023.

Wendisch, M., Crewell, S., Ehrlich, A., Herber, A., Kirbus, B., Lüpkes, C., Mech, M., Abel, S. J., Akansu, E. F., Ament, F., Aubry, C., Becker, S., Borrmann, S., Bozem, H., Brückner, M., Clemen, H.-C., Dahlke, S., Dekoutsidis, G., Delanoë, J., De La Torre Castro, E., Dorff, H., Dupuy, R., Eppers, O., Ewald, F., George, G., Gorodetskaya, I. V., Grawe, S., Groß, S., Hartmann, J., Henning, S., Hirsch, L., Jäkel, E., Joppe, P., Jourdan, O., Jurányi, Z., Karalis, M., Kellermann, M., Klingebiel, M., Lonardi, M., Lucke, J., Luebke, A. E., Maahn, M., Maherndl, N., Maturilli, M., Mayer, B., Mayer, J., Mertes, S., Michaelis, J., Michalkov, M., Mioche, G., Moser, M., Müller, H., Neggers, R., Ori, D., Paul, D., Paulus, F. M., Pilz, C., Pithan, F., Pöhlker, M., Pörtge, V., Ringel, M., Risse, N., Roberts, G. C., Rosenburg, S., Röttenbacher, J., Rückert, J., Schäfer, M., Schaefer, J., Schemann, V., Schirmacher, I., Schmidt, J., Schmidt, S., Schneider, J., Schnitt, S., Schwarz, A., Siebert, H., Sodemann, H., Sperzel, T., Spreen, G., Stevens, B., Stratmann, F., Svensson, G., Tatzelt, C., Tuch, T., Vihma, T., Voigt, C., Volkmer, L., Walbröl, A., Weber, A., Wehner, B., Wetzel, B., Wirth, M., and Zinner, T.: Overview: quasi-Lagrangian observations of Arctic air mass transformations – introduction and initial results of the HALO–$(A\ C)^3$ aircraft campaign, Atmos. Chem. Phys., 24, 8865–8892, https://doi.org/10.5194/acp-24-8865-2024, 2024.

Wendisch, M., Kirbus, B., Ori, D., Shupe, M. D., Crewell, S., Sodemann, H., and Schemann, V.: Observed and modeled Arctic airmass transformations during warm air intrusions and cold air outbreaks, Atmos. Chem. Phys., 25, 15 047–15 076, https://doi.org/10.5194/acp-25-15047-2025, 2025.

Wesche, C., Steinhage, D., and Nixdorf, U.: Polar aircraft Polar5 and Polar6 operated by the Alfred Wegener Institute, JLSRF, 2, A87, https://doi.org/10.17815/jlsrf-2-153, 2016.

Wex, H., Huang, L., Zhang, W., Hung, H., Traversi, R., Becagli, S., Sheesley, R. J., Moffett, C. E., Barrett, T. E., Bossi, R., Skov, H., Hünerbein, A., Lubitz, J., Löffler, M., Linke, O., Hartmann, M., Herenz, P., and Stratmann, F.: Annual variability of ice-nucleating particle concentrations at different Arctic locations, Atmos. Chem. Phys., 19, 5293–5311, https://doi.org/10.5194/acp-19-5293-2019, 2019.

Wood, R. and Bretherton, C. S.: On the Relationship between Stratiform Low Cloud Cover and Lower-Tropospheric Stability, Journal of Climate, 19, 6425–6432, https://doi.org/10.1175/JCLI3988.1, 2006.

Young, G., Connolly, P. J., Jones, H. M., and Choularton, T. W.: Microphysical sensitivity of coupled springtime Arctic stratocumulus to modelled primary ice over the ice pack, marginal ice, and ocean, Atmos. Chem. Phys., 17, 4209–4227, https://doi.org/10.5194/acp-17-4209-2017, 2017.